

# ROSAT PSPC observations of 36 high-luminosity clusters of galaxies: constraints on the gas fraction

S. Ettori and A.C. Fabian

Institute of Astronomy, Madingley Road, Cambridge CB3 0HA

ACCEPTED, MNRAS (1999)

## ABSTRACT

We present a detailed and homogeneous analysis of the *ROSAT* PSPC surface brightness profiles of 36 clusters of galaxies with high X-ray luminosity ( $L_X \gtrsim 10^{45}$  erg s $^{-1}$ ) and redshifts between 0.05 and 0.44. Using recent *ASCA* estimates of the temperature of the gas for most of the clusters in the sample, we apply both the deprojection technique and model fitting to the surface brightness profiles to constrain the gas and dark matter distributions under the assumption that the gas is both isothermal and hydrostatic.

Applying robust estimators, we find that the gas fraction within  $r_{500}$  of the clusters in our sample has a distribution centred on  $f_{\text{gas}}(r_{500}) = 0.168h_{50}^{-1.5}$ . The gas fraction ranges from 0.101 to 0.245 at the 95 per cent confidence level. The values of  $f_{\text{gas}}$  show highly significant variations between individual clusters, which may be explained if the dark matter has a significant baryonic component. Within a cluster, the average radial dependence of the gas mass fraction increases outward as  $r^s$ , with  $s \sim 0.20$ . Combining these results with those of primordial nucleosynthesis calculations and the current estimate of  $H_0$ , the above central location implies  $\Omega_{0,m} \lesssim 0.56$  at the 95 per cent confidence level. This upper limit decreases to 0.34 if we take the highest significant estimates for  $f_{\text{gas}}$ .

A significant decrease in cluster gas fraction with redshift from the local value,  $f_{\text{gas},0}$ , of 0.21, found assuming  $\Omega_{0,m} = 1$ , is also reduced if  $\Omega_{0,m}$  is low.

**Key words:** galaxies: cluster: general – galaxies: fundamental parameters – intergalactic medium – X-ray: galaxies – cosmology: observations – dark matter.

## 1 INTRODUCTION

The physics of the formation of clusters of galaxies depends upon the cosmological parameters,  $\Omega_{0,m}$  and  $\Omega_b$ , that describe the observed total matter density and its baryonic contribution, respectively. Assuming that clusters maintain the same ratio  $\Omega_b/\Omega_{0,m}$  as the rest of the Universe, a measure of the cluster baryon fraction can be compared with calculations from cosmic nucleosynthesis considerations of the abundance of the light elements (e.g. D,  $^3\text{He}$ ,  $^4\text{He}$ ,  $^7\text{Li}$ ) to give a direct constraint on  $\Omega_{0,m}$ .

In recent years, White et al. (1993), White & Fabian (1995), David, Jones & Forman (1995) and others have discussed this issue first for the Coma cluster and then for samples of clusters, highlighting the necessity of a low density Universe in order to reconcile the baryon fraction of the total cluster mass with the primordial  $\Omega_b \sim 0.05$ . This ‘‘Baryon Catastrophe’’ for a flat Universe persists on supercluster scales; Fabian (1991) and Ettori, Fabian & White (1997) estimate a 15 per cent gas contribution to the total

mass of the Shapley Supercluster, over a region of 30 Mpc in radius.

The main baryonic component of the richest clusters is the intracluster gas, whereas galaxies contribute less than about 4 per cent with respect to the total gravitating mass (White et al. 1993, Fukugita, Hogan & Peebles 1998). Apart from a brief discussion in Section 5, we will not consider further any other contribution to the total baryon budget in clusters, such as baryonic dark matter or cool gas, for which the uncertainties are still large (cf. Fukugita et al. 1998). Thus, the gas fraction provides a lower limit on the total baryon fraction in clusters.

The information on the gas and total mass distributions is inferred from spectral and spatial analyses in the X-ray waveband. To properly know the gas density, we need to deproject the observed surface brightness profile, which is simply the projection on the sky of the (mostly)

arXiv:astro-ph/9901304v2 15 Apr 1999

bremstrahlung<sup>\*</sup> emissivity,  $\epsilon \propto (\text{cluster plasma temperature, } T_{\text{gas}})^{1/2} \times (\text{gas density, } \rho_{\text{gas}})^2$  (for  $T_{\text{gas}} \gtrsim 3 \times 10^7$  K; see e.g. Rybicki & Lightman 1979), i.e.:

$$S(b) = \int_{b^2}^{\infty} \frac{\epsilon dr^2}{\sqrt{r^2 - b^2}}. \quad (1)$$

Due to the small dependence of  $S(b)$  on the temperature (in particular in the *ROSAT* waveband),  $\rho_{\text{gas}}$  is well constrained from eqn. 1. Assuming that the hydrostatic equilibrium holds in the cluster regions examined, we can write:

$$\frac{1}{\rho_{\text{gas}}} \frac{dP_{\text{gas}}}{dr} = -\frac{d\phi}{dr} = -\frac{GM_{\text{tot}}(r)}{r^2}, \quad (2)$$

where  $G$  is the gravitational constant, and the gas pressure,  $P_{\text{gas}}$ , is calculated through the perfect gas law,  $P_{\text{gas}} = \rho_{\text{gas}} k T_{\text{gas}} / (\mu m_{\text{p}})$  (the mean molecular weight,  $\mu$ , is 0.6 in atomic mass unit). At the present, there are two unknown quantities: the temperature profile (for sake of simplicity we assume the gas to be isothermal, but see Sect. 4.3) and the dark matter distribution. Fixing one of these allows us to solve the differential equation for the other one. In particular, according to the different cases that we discuss in Sect. 3, we adopt the dark matter density profile found in N-body simulations and the best available estimate of the intracluster temperature,  $T_{\text{gas}}$ .

In this paper, we present the analysis of *ROSAT* Position Sensitive Proportional Counter (PSPC) surface brightness profiles of 36 clusters of galaxies, with X-ray luminosity greater than  $10^{45}$  erg s<sup>-1</sup> and redshift in the range 0.05-0.44. These physical characteristics allow them to be well covered by the PSPC field of view, with the surface brightness profile extending to about the virial radius.

Due to the energy-limited range of the PSPC (0.1–2.4 keV), we use observations of  $T_{\text{gas}}$  from recent published work on *ASCA* data (0.5–10 keV).

The paper is organized as follows. In Section 2, we present the cluster sample and data reduction methods. In Section 3, we obtain constraints on the cluster dark matter after comparing the deprojection analysis with a straightforward fitting approach, using both a  $\beta$ -model and a gas profile obtained through the Navarro-Frenk-White dark matter profile. In Section 4, the value and the distribution of the gas fraction,  $f_{\text{gas}}$ , are discussed. The constraints that we place on  $\Omega_{0,m}$  using the best estimate of  $f_{\text{gas}}$ , and the primordial nucleosynthesis results, are presented in Section 5. We summarize our main results in Section 6.

## 2 THE SAMPLE

We have compared samples of clusters of known X-ray luminosity (David et al. 1993, White et al. 1997, Markevitch 1998, Allen & Fabian 1998) with the *ROSAT* archive in order to select observations of bright luminous clusters ( $L_X > 10^{45}$  erg s<sup>-1</sup>) at moderate redshifts ( $z > 0.05$ ). This optimises analysis of the distribution of the gas in the outer regions of each cluster.

\* We adopt a *MEKAL* model for our analysis as described in Sect. 3

Furthermore, we have not considered clusters that, although matching the selection criteria presented above, either have evidence of a major merger that affects both the determination of the centre and the hydrostatic equilibrium, like Cygnus-A (Owen et al. 1997), A754 (Henriksen & Markevitch 1996), A2255 (Davis & White 1998), A3667 (Rottgering et al. 1997) or are part of larger and more complex system (e.g. A85, Durret et al. 1998).

Here we note that this sample is not complete in any sense: for example, if we consider the X-ray-brightest Abell-type clusters sample (XBACs, Ebeling et al. 1996), that is complete at the 80 per cent up to redshift of 0.2 for flux in the *ROSAT* band (0.1 – 2.4 keV) larger than  $5 \times 10^{-12}$  erg cm<sup>-2</sup> s<sup>-1</sup>, and make the same selection done here, we find 110 items. Of these, 28 are in common with our sample, 53 are not available in the *ROSAT* archive, 19 have only HRI images, 8 have PSPC data but no information on the gas temperature and 2 are now confirmed with  $L_{X,\text{bol}} < 10^{45}$  erg s<sup>-1</sup>.

In Table 1, we present the list of the selected clusters with their basic physical parameters. The intracluster temperatures,  $T_{\text{gas}}$ , come from published spectral analyses. The clusters in our sample are very luminous hot objects for which only observatories with a wide X-ray energy band, like *GINGA* and *ASCA*, can properly measure temperatures using the hard tail of the X-ray spectrum. We therefore use *ASCA* measurements for all the clusters apart from A483 and A2507 (*GINGA* data), A3112 (*EXOSAT*), A545, A2244 (*Einstein* MPC), and A3888 (from its optical velocity dispersion).

In particular, we are interested in the temperature of the bulk of the cluster gas, possibly not affected from the presence of any cooling central gas, which can lead to a lower (emission-weighted) temperature. Thus, in the following analysis, we consider gas temperatures that have measured either excluding the core region (Markevitch 1998) or including a cooling flow component in the spectral fit (Allen & Fabian 1998).

The error bars on the temperatures quoted in Table 1 are *symmetric*  $1\sigma$  uncertainties. When the published source reports asymmetric errors at the 90 per cent confidence level, we consider the largest value and divide by 1.64 (this assumes that the errors are Gaussian).

The *PSPC* images have been constructed from counts in the 0.5-2 keV band, where the Galactic and particle background are minimum, after correction for instrumental and telemetry dead time, exclusion of times of high background counts. We also require the Master Veto count rate to be less than 170 counts s<sup>-1</sup> (cf. guidelines for reduction of PSPC data in Snowden et al. 1994). Using the *ROSAT* Interactive Data Language (IDL) user-supplied libraries, we have divided the images by the respective exposure maps in the same energy band and corrected them for vignetting and exposure-time. The region of the detector support rib has been masked out as well all detected point sources. The clusters examined do not show evidence for a major merger, but may be affected by low level substructure. These clumps have also been masked despite their small contribution to the total flux.

The surface brightness profiles have been extracted by estimating the X-ray centre from the exposure-corrected image after smoothing by a median filter of width of 5 pixels.

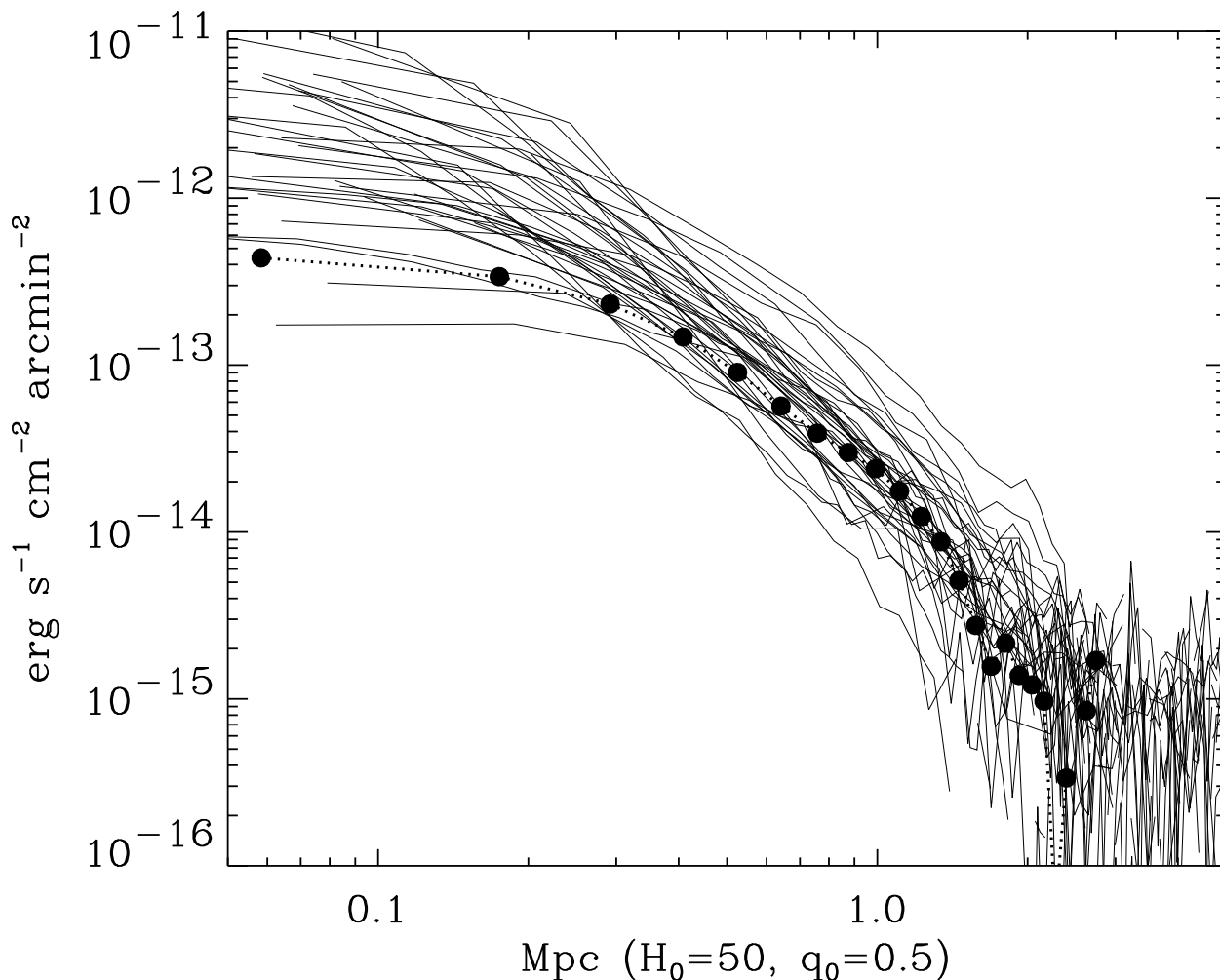


**Figure 1.** The surface brightness profiles of the clusters in our sample in the 0.5-2 keV band, converted to the flux at the rest-frame energy band and corrected for the cosmological dimming by a factor  $(1+z)^4$ , are here compared with the Coma profile (dots connected by dotted line).

The background has been calculated as an average of the counts  $\text{s}^{-1} \text{ arcmin}^{-2}$  present between  $40'$  and  $45'$  in a sector which has no significant contamination from non-cluster emission (cf. column “bkg” in Table 1).

The outer radius,  $R_{\text{out}}$  (Table 1), of the extracted and background-subtracted profile is defined as the maximum radius where the signal exceeds twice the error present in that radial bin. This error is calculated by adding in quadrature the Poisson errors on the photon counts both in that bin and the background.

The bin size, of at least 30 arcsec to avoid any effect of the Point-Spread-Function, is chosen to improve the signal-to-noise ratio in the outskirts of the cluster. In clusters where an improvement is significant, we quote in Table 1 values for bin sizes larger than 30 arcsec.

Fig. 1 plots all the surface brightness profiles (in counts  $\text{s}^{-1} \text{ arcmin}^{-2}$ ) against radius (in Mpc). We convert from the angular size to the physical dimension in each cluster, using the following equation for angular distance

$$r(\text{Mpc}) = 87.21 r(\text{arcmin}) \frac{q_0 z + (q_0 - 1)(\sqrt{2q_0 z + 1} - 1)}{H_0 q_0^2 (1+z)^2}. \quad (3)$$

We use, as cosmological parameters  $(H_0, q_0)$ , the values  $(50 \text{ km s}^{-1} \text{ Mpc}^{-1}, 0.5)$ .

Here we note that this proper radius is inversely proportional to  $H_0$  and depends slightly upon  $q_0$  (a variation of 5 per cent is observed on changing  $q_0$  from 0.5 to 0.01 in the redshift range 0.01–0.4, with the larger deviation of about 10 per cent at the highest redshifts). We discuss further in Section 4 the cosmological dependence of the proper radius,  $r$ .

### 3 DEPROJECTION AND FITTING ANALYSIS

We analyse the surface brightness profiles to determine the distribution of the gas density in the clusters through the two usual techniques, i.e. by fitting the surface brightness profile and by deprojecting it. Both techniques make the

**Table 1.** ROSAT observation summary. Reference: [1] Allen & Fabian (1997); [2] Böhringer et al. (1998); [3] David et al. (1993); [4] Fukazawa et al. (1998); [5] Markevitch (1998); [6] from  $T_X - \sigma_{\text{opt}}$  relation in White, Jones & Forman (1997) and  $\sigma_{\text{opt}} = 1307 \pm 100 \text{ km s}^{-1}$  (Girardi et al. 1997). *Note:* A2142 = rp800233 +wp800551n00 +wp800096 +wp150084.  $R_{\text{out}}$  is in Mpc, ‘bkg’ is in units of  $10^{-4} \text{ count s}^{-1} \text{ arcmin}^{-2}$ .  $\dagger$  This value (in units of  $10^{20} \text{ atoms cm}^{-2}$ ) is the average of the HI column density, calculated within 1 degree and weighted with respect to the distance from the quoted coordinates (from the map by Dickey & Lockman 1990).

cluster	Seq. Id.	Exp. (ks)	$z$	$\alpha_{2000}$	$\delta_{2000}$	$N_{\text{H}}^{\dagger}$	$T_{\text{gas}}$ (keV)	bin	$R_{\text{out}}$	bkg
A401	rp800235n00	6.6	0.0748	02 <sup>h</sup> 58 <sup>m</sup> 56 <sup>s</sup> .1	+13° 34′ 55″	10.5	$8.0 \pm 0.2$ [5]	30″-57.5 kpc	2.10	2.18
A478	rp800193n00	21.8	0.0881	04 13 23.9	+10 28 04	15.1	$8.1 \pm 0.7$ [1]	60-132.5	2.05	1.86
A483	rp800089n00	9.7	0.2800	04 15 54.8	-11 32 17	3.9	$8.7 \pm 2.0$ [3]	30-158.2	1.19	5.53
A520	rp800480n00	4.6	0.2030	04 54 08.2	+02 55 42	7.8	$8.3 \pm 0.5$ [1]	30-128.0	1.86	2.43
A545	rp800523n00	13.2	0.1530	05 32 24.0	-11 32 15	11.5	$5.5 \pm 6.2$ [3]	90-311.8	2.34	1.93
A586	rp800348n00	2.9	0.1710	07 32 18.6	+31 38 19	5.2	$10.7 \pm 6.3$ [1]	30-113.0	1.19	2.25
A644	rp800379n00	8.7	0.0704	08 17 24.5	-07 30 29	6.8	$8.1 \pm 0.5$ [5]	90-163.5	3.02	1.99
A665	rp800022n00	34.1	0.1816	08 30 56.3	+65 50 52	4.2	$9.0 \pm 0.4$ [1]	60-236.3	2.24	3.54
A1068	rp800410n00	9.5	0.1386	10 40 42.6	+39 57 22	1.0	$5.5 \pm 0.9$ [1]	30-96.3	1.20	2.27
A1413	rp800183n00	7.1	0.1427	11 55 17.6	+23 24 28	2.2	$8.5 \pm 0.8$ [1]	30-98.5	1.53	3.05
A1651	wp800353	7.1	0.0825	12 59 20.6	-04 11 30	1.8	$6.1 \pm 0.2$ [5]	90-187.8	2.91	3.01
A1689	rp800248n00	12.9	0.1810	13 11 28.7	-01 20 17	1.8	$10.0 \pm 0.7$ [1]	30-117.9	1.59	3.06
A1763	rp800252n00	12.2	0.1870	13 35 17.0	+41 00 07	0.9	$9.7 \pm 0.4$ [1]	60-241.4	2.05	2.72
A1795	rp800105n00	34.4	0.0621	13 48 51.3	+26 35 46	1.2	$5.9 \pm 0.2$ [1]	30-48.7	1.49	3.66
A1835	rp800569n00	6.0	0.2523	14 01 00.9	+02 53 10	2.3	$9.8 \pm 1.4$ [1]	30-148.2	1.41	3.16
A2029	rp800249n00	9.7	0.0765	15 10 54.7	+05 45 07	3.0	$8.5 \pm 0.2$ [1]	60-117.3	2.17	5.24
A2142	[see note]	18.9	0.0899	15 58 18.3	+27 14 07	4.2	$9.3 \pm 0.8$ [1]	60-134.8	2.49	3.18
A2163	wp800385	6.8	0.2030	16 15 44.6	-06 08 45	12.1	$13.8 \pm 0.5$ [1]	30-128.0	2.37	3.77
A2204	rp800281n00	5.2	0.1523	16 32 46.1	+05 34 55	5.7	$9.2 \pm 1.5$ [1]	30-103.6	1.50	9.37
A2218	rp800097n00	34.9	0.1750	16 35 49.3	+66 12 58	3.2	$7.1 \pm 0.2$ [1]	30-115.0	2.01	3.68
A2219	rp800571n00	8.0	0.2280	16 40 17.5	+46 42 58	1.8	$12.4 \pm 0.5$ [1]	30-138.6	2.29	2.70
A2244	rp800265n00	2.8	0.0970	17 02 40.2	+34 03 37	2.1	$7.1 \pm 2.4$ [3]	30-71.9	1.40	3.00
A2256	rp100110n00	16.1	0.0581	17 03 08.1	+78 39 19	4.1	$7.1 \pm 0.2$ [5]	30-45.9	2.50	2.71
A2319	rp800073a01	2.6	0.0559	19 21 09.9	+43 56 58	7.9	$9.3 \pm 0.2$ [1]	60-88.6	2.61	3.26
A2390	wp800570n00	8.3	0.2279	21 53 35.1	+17 42 06	6.8	$11.1 \pm 1.0$ [2]	30-138.6	2.01	2.92
A2507	rp800088n00	4.8	0.1960	22 56 49.8	+05 30 28	5.6	$9.4 \pm 1.6$ [3]	30-124.8	1.69	2.28
A2744	rp800343n00	13.3	0.3080	00 14 17.5	-30 23 32	1.6	$11.0 \pm 0.5$ [1]	30-167.5	1.42	3.27
A3112	rp800302n00	6.7	0.0746	03 17 55.6	-44 13 56	2.6	$4.1 \pm 1.4$ [3]	30-57.4	1.35	2.99
A3266	wp800552n00	12.7	0.0594	04 31 15.9	-61 26 48	1.6	$8.0 \pm 0.3$ [5]	30-46.8	2.04	3.53
A3888	rp700448n00	4.0	0.1680	22 34 26.3	-37 43 50	1.2	$(9.0 \pm 1.2)$ [6]	30-111.6	1.28	5.85
IRAS 09104	rp701555n00	5.8	0.4420	09 13 45.2	+40 56 31	1.0	$8.5 \pm 3.4$ [1]	60-404.6	1.42	2.04
MS 1358	rp800109n00	18.4	0.3290	13 59 49.4	+62 31 19	1.9	$7.5 \pm 4.3$ [1]	60-347.9	1.22	3.44
MS 2137	rp800573n00	8.8	0.3130	21 40 13.9	-23 39 29	3.6	$5.2 \pm 1.1$ [1]	30-169.1	1.10	2.98
PKS 0745	wp800623n00	7.4	0.1028	07 47 30.1	-19 17 09	46.6	$8.7 \pm 1.0$ [1]	30-75.5	1.93	2.14
Triang. Aus.	rp800280n00	6.4	0.0510	16 38 20.4	-64 21 14	13.0	$10.1 \pm 0.7$ [4]	30-40.8	2.41	4.27
Zw 3146	rp800520n00	7.9	0.2906	10 23 39.3	+04 11 31	3.0	$11.3 \pm 3.5$ [1]	30-161.8	1.05	2.88

reasonable assumption that the observed projected cluster emission is due to X-ray emitting gas which is spherically symmetric. In particular, the former assumes a model for the gas density, projects it on the sky and fits it to the data to constrain the parameters of the model; the latter, the deprojection technique, makes a proper geometrical deprojection of the profile and determines the gas density and temperature profile, assuming a dark matter distribution.

In the next two subsections, we present these two methods and the results obtained on the distribution of the intracluster gas. In the last subsection, the constraints on the dark matter in the case of the hydrostatic equilibrium are discussed.

### 3.1 Fitting approach

We have adopted here the following two models for the gas density and the projected surface brightness profile:

(i) a single  $\beta$ -model (Cavaliere & Fusco-Femiano 1976),

$$\rho_{\text{gas}} = \rho_0 \left[ 1 + \left( \frac{r}{r_c} \right)^2 \right]^{-1.5\beta} \rightarrow S_b = S_0 \left[ 1 + \left( \frac{r}{r_c} \right)^2 \right]^{0.5-3\beta} ; (4)$$

(ii) a gas density profile obtained using the Navarro, Frenk & White (1997; hereafter NFW) dark matter profile in the hydrostatic equation where the gas is assumed isothermal (cf. Appendix; a first application on the Perseus cluster is presented in Ettori, Fabian & White 1998; a first theoretical discussion is found in Makino et al. 1998):

$$\rho_{\text{gas}} = a_0(1+x)^{\eta/x}, (5)$$

where  $x = r/r_s$ ,  $\eta = 4\pi G \rho_s r_s^2 \mu m_p / (kT_{\text{gas}})$  and  $\rho_s = \rho_c \delta_c (1+z)^3 \Omega_0 / \Omega_z$ , with  $\delta_c$  equal to the characteristic density of the cluster and  $\rho_c$  to the critical density (see Appendix in Navarro, Frenk & White 1997).

The surface brightness profile is then obtained by numerical integration of the gas density through equation 1.

All the fits have been performed by a non-linear least squares technique (routine *Curvefit* in IDL). This algorithm, however, is sensitive to large departures for a (generally small) number of data points, the so-called *outlier points*. A statistical estimator that is able to properly weight these points is qualified as robust. Thus, we have also tested our results with a robust estimator of the minimization of the function  $(y[\text{raw data}] - y[\text{fit}])/\sigma[\text{raw data}]$ , namely the downhill simplex method implemented in the *amoeba* routine (Press et al. 1992; IDL vers. 5.0). Generally, the agreement is good (with a deviation of the best estimate of the parameters of about 1 per cent in average) due to the large number of radial bins available.

In the following analysis, we present the results obtained from the robust estimate of the model parameters. We show in Fig. 2 the count distribution of the values of the  $\beta$ -model parameters,  $(r_c, \beta)$ , and for the NFW gas profile,  $(r_s, \eta)$ . In this figure, we overplot the best-fit results obtained over the radial range  $[0, R_{\text{out}}]$  and  $[0.2, R_{\text{out}}]$  Mpc. The choice of the second radial range avoids any cooling flow (if present in the inner part of the cluster) on the estimates of the parameters. Doing this, we measure [average, dispersion] best-fit values of  $r_c = [0.29, 0.19]$  Mpc,  $\beta = [0.72, 0.09]$ , and  $r_s = [0.95, 0.67]$  Mpc,  $\eta = [10.29, 1.55]$ .

A range of tests to check whether the two sample populations, histograms for which are plotted in Fig. 2, have significantly different mean and/or variance, shows disagreement at 95 per cent confidence level of the variance (“F-variance test”) in the populations of  $\beta$  and  $\eta$ .

With the intention to link the results of the fit using both the  $\beta$ -model and the NFW profile, we perform a linear unweighted polynomial fit on the grid of parameters (Fig. 3). We obtain  $r_s = 3.17 r_c$  and  $\eta = 14.34 \beta$ . These correlations are consistent with the best-fit results, when one model is fitted with the other (cf. also Makino et al. 1998).

In the following analysis, we use the results from the fit with the NFW gas profile. A comparison between the two fits shows that the NFW gas profile provides a  $\chi^2$  lower than the value from the  $\beta$ -model in 19 out of 36 clusters. Furthermore, even if the fit with the NFW gas profile is computationally more expensive, we show in the Appendix that its best-fit parameters are directly linked with the scale radius and normalization of the dark matter profile obtained from N-body simulations.

In particular, as we discuss in Section 3.3, we are interested in defining in each cluster the radius,  $r_{500}$ , where the overdensity of the dark matter with respect to the average value is 500. Hence, after we have measured the best-fit parameters in  $[0.2, R_{\text{out}}]$  Mpc, we calculate  $r_{500}$  and, for only those clusters in which  $r_{500} < R_{\text{out}}$ , reiterate the fit over the range  $[0.1, 1] r_{500}$  until the convergency on  $r_{500}$  is reached, i.e. the estimated value of  $r_{500}$  is within 0.01 Mpc. A maximum of 3 trials is required to converge.

The corresponding best fit values are quoted in Table 2 and then used to describe the gas distribution through the deprojection of the central density. Using XSPEC (vers.10, Arnaud 1996), we have converted the fitted count rates to the flux due to thermal X-ray emission from an optically-thin plasma [*MEKAL* code, based on the model calculations of Mewe and Kaastra (Kaastra 1992) with Fe L calculations by Liedahl (1995)], assumed isothermal at the temperature given in Table 1, with a fixed metallicity of 0.4 times so-

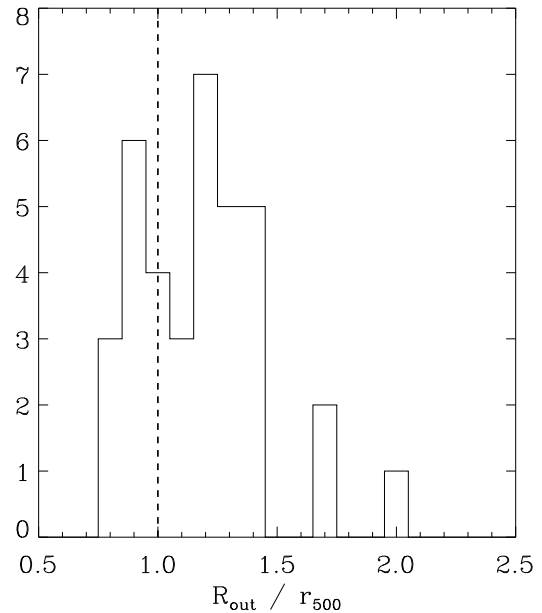


**Figure 4.** The histogram for  $R_{\text{out}}/r_{500}$  provides an indication of the region ‘seen’ with respect to the extrapolated one. Values for this ratio greater than, or equal to, 1 confirm that our profiles can trace the mass within an overdensity in dark matter of 500. This happens in 23 of the 36 clusters (64 per cent).

lar abundance, and with Galactic absorption included (cf. Table 1).

### 3.2 Deprojection procedure

In the deprojection technique, the count emissivity in each radial volume shell is calculated analytically and compared with the predicted counts from the emission predicted from an optically thin gas (described by a *MEKAL* model) absorbed by intervening matter ( $N_{\text{H}}$  from Table 1) and convolved with the response of the detector. After selecting boundary condition (i.e. the pressure in the outermost bin which allows the resulting deprojected temperature profile to match the observationally determined cluster temperature), the gas temperature and density profiles are obtained, once a model for the dark matter distribution is defined (see White, Jones & Forman 1997 for a detailed discussion on the deprojection technique).

The gravitational potential is described by a functional form given by the sum of two contributions: the central galaxy potential parametrised by a de Vaucoulers law (1948), assumed fixed for all the clusters and with parameters  $R_{\text{eff}} = 30$  kpc and velocity dispersion of  $300 \text{ km s}^{-1}$  (Malumuth & Kirshner 1985), and a Navarro-Frenk-White potential for the general cluster. The latter potential has a scale parameter, *core*, and a velocity dispersion,  $\sigma_{\text{DM}}$ , which is well represented, under the isothermal assumption, by the intracluster temperature  $[\sigma_{\text{DM}} = (kT_{\text{gas}}/\mu m_{\text{p}})^{0.5}]$ ; cf. Table 2].

For some clusters with  $T_{\text{gas}}$  larger than 10 keV, for which the temperature determination is not very precise (e.g. A2163, A2744), we fix  $\sigma_{\text{DM}}$  to the optical estimate of

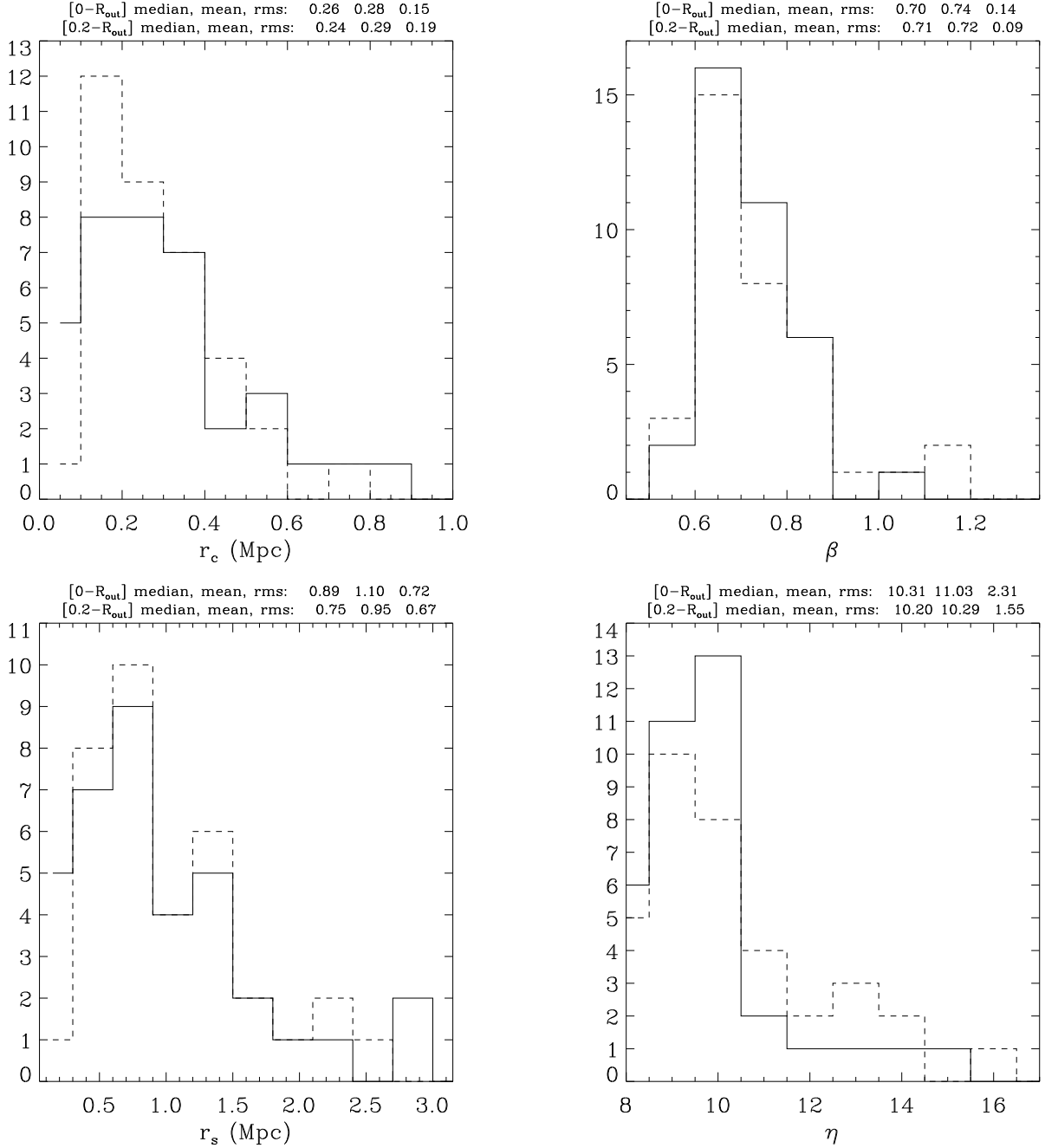


**Figure 2.** Histograms of the parameters from the  $\beta$ -model and NFW gas profile. The histograms of the best-fit parameters in the range  $[0.2 - R_{\text{out}}]$  and  $[0 - R_{\text{out}}]$  are with *solid* and *dashed* line, respectively. The median, mean and standard deviation for each distribution is quoted in the title of each plot.

the velocity dispersion and require a flat temperature profile. The required values for the velocity dispersion are larger than the predicted one from the isothermal relation by 15 and 50 per cent, for A2163 and A2744, respectively.

### 3.3 The total gravitating mass

From the fits on the surface brightness profile, and the de-projections, we obtain constraints on the gas density distri-

bution under the assumption of an isothermal plasma in a spherically symmetric cluster.

To do this, we have assumed a functional form for the total matter density and applied the hydrostatic equilibrium written in equation 2. The distribution of the total gravitating mass is then obtained through the radial integration of the total matter density profile.

We recall that our estimates of the total mass,  $M_{\text{tot}}(< r)$ , are based upon (i) radial surface brightness profiles that reach a median  $R_{\text{out}}$  of 1.93 Mpc, (ii) gas temperatures that

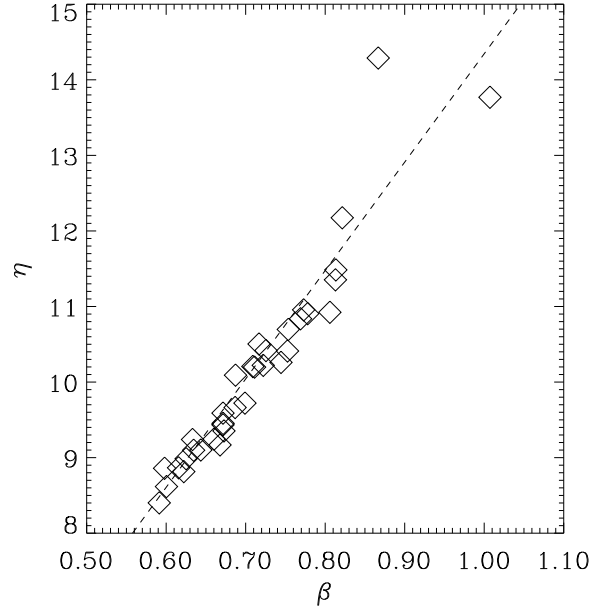
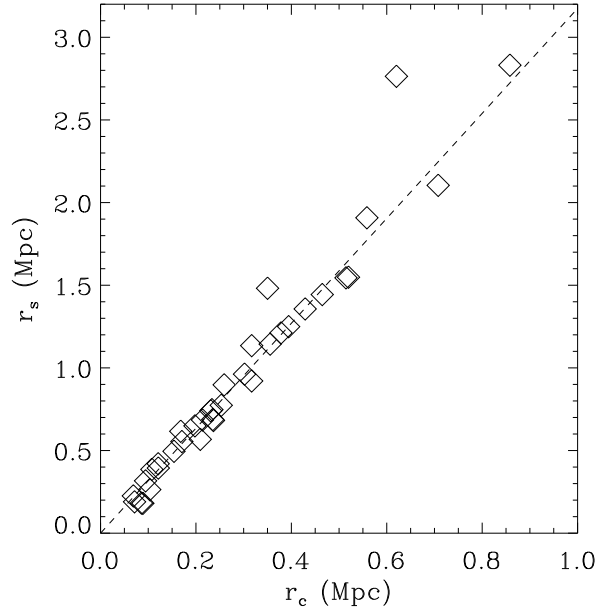


**Figure 3.** Correlations between the scale and slope parameters in the  $\beta$ -model and NFW gas profile.

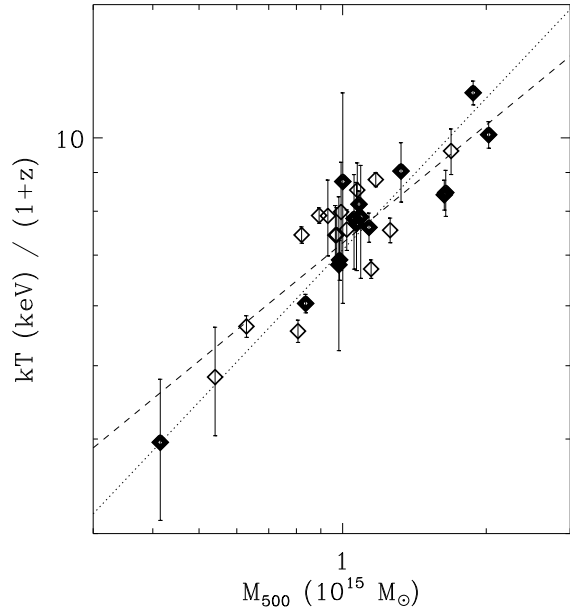


**Figure 5.** This plot shows the gas temperature vs.  $M_{500}$  with the best-fit power law functions: (*dotted line*)  $M_{500} = 1.67(\pm 0.02) (T/10 \text{ keV})^{1.5} 10^{15} M_{\odot}$  ( $\chi^2 = 212$ , with 29 degree-of-freedom); (*dashed line*)  $M_{500} = 1.86(\pm 0.04) (T/10 \text{ keV})^{1.93 \pm 0.09} 10^{15} M_{\odot}$  ( $\chi^2 = 184$ , with 28 degree-of-freedom). The clusters at high redshift, with respect to the median value, are the solid symbols.

both are corrected for any cool component in the core and were measured from broad-band detectors that describe well the shape of the thermal emission from the clusters, (iii) the

assumption that the gas is isothermal (but see considerations in Sect. 4.3).

This last assumption seems reasonable and conservative from recent results on simulations of gas dynamics (Evrard, Metzler & Navarro 1996), if one considers regions of the clusters where the overdensity of dark matter with respect to the average value is 500. Thus, we quote in the following analysis the value of the radius,  $r_{500}$ , where this overdensity is reached, and  $M_{\text{tot}}(< r_{500}) = M_{500}$  using the best-fit parameters of the NFW gas density profile and the relations discussed in the Appendix.

Considering that we obtain a median value for  $r_{500}$  of 1.66 Mpc to be compared to a median  $R_{\text{out}}$  of 1.93 Mpc (cf. Fig. 4), the proper gravitating mass for each cluster is here determined in a robust way, generally without any extrapolation or application of either the  $r - T_{\text{gas}}$  or  $M_{\text{tot}} - T_{\text{gas}}$  relation (Evrard et al. 1996, Hjorth, Oukbir & van Kampen 1998), which would need a proper calibration through independent measurements of the mass (e.g. hydrodynamics simulations, gravitational lensing) and replaces the peculiarity of a cluster with an average behaviour.

For comparison with previous work, we have also investigated the  $M_{500} - T_{\text{gas}}$  relation, after calculating  $M_{500}$  for the 30 clusters of our final sample (see next section). Adopting the scaling relation  $M \propto r T_{\text{gas}} \propto T_{\text{gas}}^{3/2} (1+z)^{-3/2}$ , where the last step implies that  $r \propto M^{1/3} (1+z)^{-1}$ , we obtain a best-fit of  $M_{500} = 1.67(\pm 0.02) [T_{10, \text{gas}} / (1+z)]^{1.5} \times 10^{15} M_{\odot}$ , where  $T_{10, \text{gas}}$  is in units of 10 keV (Fig. 5). Leaving as free parameter the slope of the temperature, we measure  $M_{500} = 1.86(\pm 0.04) [T_{10, \text{gas}} / (1+z)]^{1.93 \pm 0.09}$ , slightly steeper than a power law with index of 1.5.

At  $r_{500}$ , Evrard (1997) measures from simulated clusters a coefficient  $2.22 \pm 0.32$  for the above relation. The disagreement with our best-fit result is due mainly, apart from the

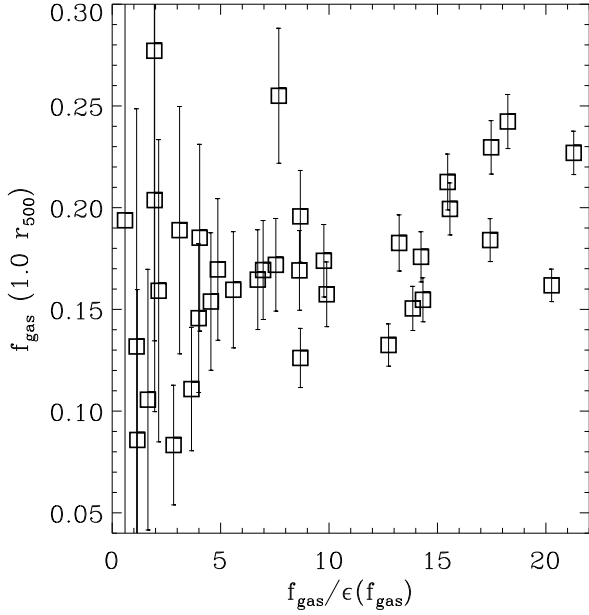


**Figure 7.** The gas mass fraction values for our 36 clusters are plotted versus the ratio  $f_{\text{gas}}/\epsilon(f_{\text{gas}})$ . Only the 30 clusters with  $f_{\text{gas}}/\epsilon(f_{\text{gas}}) > 2$  have been considered in our final sample.

large scatter, to the steeper gas profiles predicted by the simulations.

#### 4 THE GAS FRACTION

The standard primordial nucleosynthesis theory indicates the present universal ratio of baryons to photons as the free parameter to be constrained through the observations of the abundances of the light-elements. Once the microwave background temperature is fixed, and models with three light neutrinos adopted, one can estimate the baryonic mass density in units of the critical density,  $\Omega_b = \rho_b/\rho_c$ . Recently, conflicting estimates of the abundance of deuterium, D, have raised questions on the robustness of a general value for  $\Omega_b$  (e.g. Hogan 1997). A high D abundance agrees with  $^4\text{He}$  and  $^7\text{Li}$  measurements and with the baryonic cosmic budget (Fukugita et al. 1998) and constrains  $\Omega_b h_{50}^2$  between 0.020 and 0.064 (with a central value of about 0.04; e.g. Songaila, Wampler & Cowie 1997), on the other hand a low D/H ratio match Galactic chemical evolution and local measurements better. In this case,  $\Omega_b h_{50}^2$  is  $0.076 \pm 0.004$  (cf. Burles & Tytler 1997).

Thus, if regions that collapse to form rich clusters in an Einstein-de Sitter Universe retain the same value of  $\Omega_b$  as the rest of the Universe, only a few per cent of cluster masses can be due to baryons (mostly gas in the ICM, but also stars in galaxies and eventual dark and cool baryons), in opposition with the observed 10–30 per cent (Briel et al. 1992, White et al. 1993, White & Fabian 1995, David, Jones & Forman 1995, this paper).

It is worth noting that, historically, X-ray observations have always shown a relatively high baryon fraction in clusters (e.g. Stewart et al. 1984); White & Frenk (1991) high-

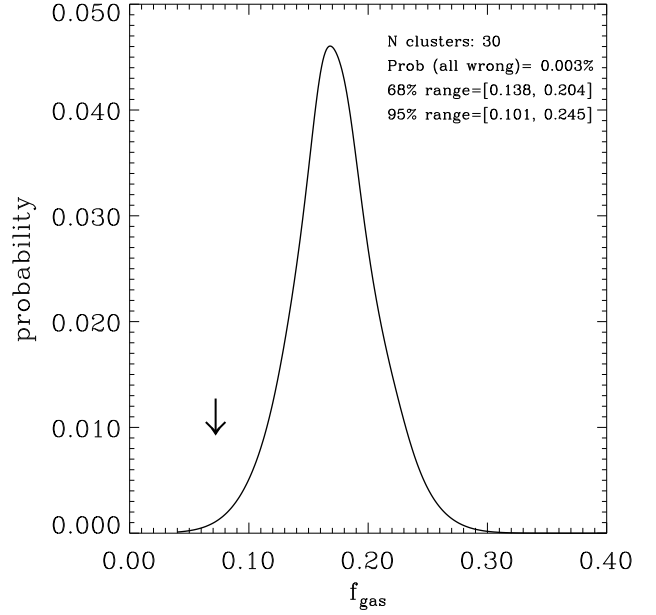


**Figure 8.** Bayesian probability distribution for the gas fraction observed in the clusters in our refined sample. This distribution peaks at  $f_{\text{gas}} = 0.168$ . The arrow indicates the constraints from the primordial nucleosynthesis value for the low D/H case. It has a probability of  $7.2 \times 10^{-3}$  with respect to the plotted distribution.

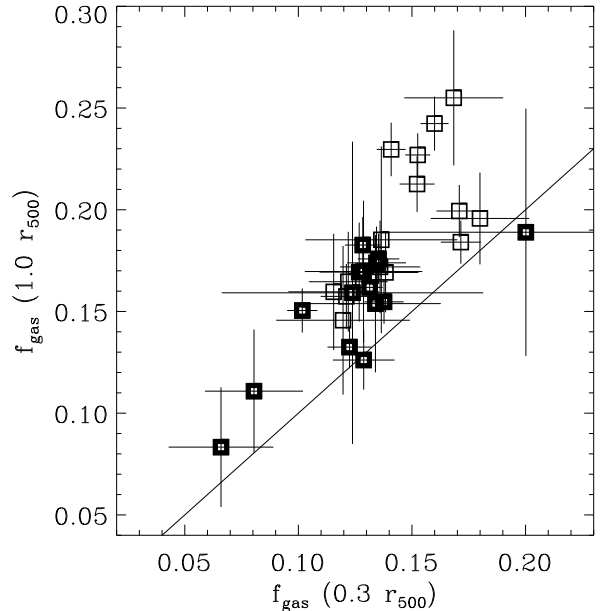


**Figure 9.** The gas fraction compared at different radii, i.e. at 0.3 and 1  $r_{500}$ . This corresponds to about 0.5 and 1.7 Mpc, if we consider the median value of our sample of 36 clusters. The solid line indicates  $f_{\text{gas}}(0.3 r_{500}) = f_{\text{gas}}(1.0 r_{500})$ . Most of the clusters show an excess in the gas contribution at larger radii. The clusters at high redshift, with respect to the median value, are the solid symbols.



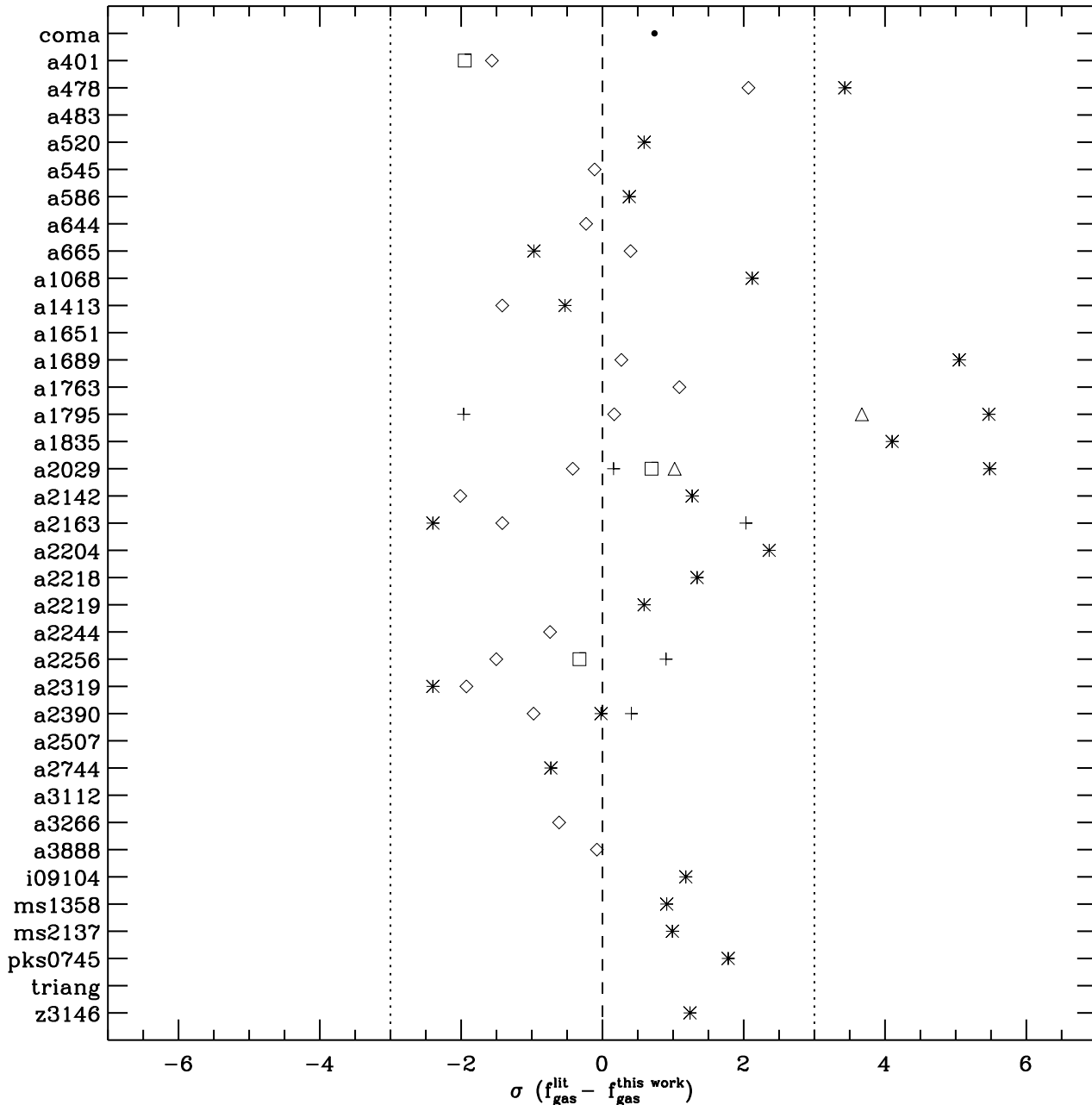


**Figure 6.** Plot of the difference in standard deviation between  $f_{\text{gas}}$  from published sources and our estimate for each cluster in our sample. We compare the data at the same radius and using the same technique [i.e. the deprojection for the results from Allen & Fabian (1998) and White et al. (1997)]. For the White et al. (1997) results, we propagate the uncertainties on the “reprojected” gas temperature to the total mass. We include also the Coma cluster as comparison. Note:  $\bullet$ , White et al. (1993; at  $r = 3$  Mpc);  $+$ , A1795: Briel & Henry (1996; at  $r = 1$  Mpc), A2029: Sarazin et al. (1998; at  $r = 1.88$  Mpc), A2163: Elbaz, Arnaud & Böhringer (1995; at  $r = 1.5$  Mpc), A2256: Markevitch & Vikhlinin (1997; at  $r = 3$  Mpc), A2390: Böhringer et al. (1998; at  $r = 1$  Mpc);  $*$ , Allen & Fabian (1998; at  $r = 0.5$  Mpc);  $\diamond$ , White, Jones & Forman (1997, up-to-date version of White & Fabian 1995; at  $r = 1$  Mpc);  $\triangle$ , David, Jones & Forman (1995; at  $r = r_{500}$ );  $\square$ , Buote & Canizares (1996, but after corrections on the total masses [Buote, priv. comm.]; at  $r = 1$  Mpc).

lighted the discrepancy for the Coma cluster when new tighter and lower constraints from nucleosynthesis were published by Walker et al. (1991).

In our case, the gas fraction,  $f_{\text{gas}}$ , is estimated by the ratio of the gas mass determined in the deprojection (and fitting) analysis to the gravitational mass estimated through

the hydrostatic equation. The measured values of  $f_{\text{gas}}$  at 0.5, 1, 1.5 Mpc (where available, i.e. for radii less than  $R_{\text{out}}$  and  $r_{500}$  (from the best-fit parameters of the NFW gas density profile) are quoted in Table 2.

All the values quoted at  $r_{500}$  are obtained using the best fit parameters as described in Sect. 3.1. The 68 per

**Table 2.** This table contains the dark matter parameters used in the deprojection analysis, the best-fit parameters from the fitting procedure, the value of  $r_{500}$  as measured applying the NFW gas profile, and the gas fraction from the deprojection analysis calculated, where available (i.e. for radii less than  $R_{\text{out}}$ ; cf. Table 1), at the bin closest to the quoted radius. In *italics* we quote  $f_{\text{gas}}$  as measured at that radius by the fitting method. The value of  $f_{\text{gas}}(r_{500})$  is obtained by using the best-fit parameters with the NFW profile. *Note:* core,  $r_c, r_s, r_{500}$  in Mpc;  $\sigma_{\text{DM}}$  in  $\text{km s}^{-1}$ . In the first column, we quote in parenthesis  $\sigma_{\text{DM}}$  as calculated from  $T_{\text{gas}}$  assuming the isothermal condition. <sup>†</sup> from optical analysis in Struble & Rood (1991; A2163), Smail et al. (1997; A2744).

cluster	DEPROJ	FITTING				$f_{\text{gas}}$			
	core, $\sigma_{\text{DM}}$	$r_s, \eta$	$r_c, \beta$	$r_{500}$	< 0.5 Mpc	< 1.0 Mpc	< 1.5 Mpc	< $r_{500}$	
A401	0.90 1100 (1103)	0.62 8.17	0.22 0.59	1.66	0.160 0.007 (0.141)	0.194 0.010 (0.187)	0.223 0.013 (0.220)	0.230 0.013	
A478	0.40 1100 (1110)	0.46 9.56	0.17 0.69	1.73	0.130 0.017 (0.135)	0.157 0.020 (0.153)	0.171 0.022 (0.166)	0.172 0.023	
A483	0.80 1150 (1150)	1.13 10.50	0.32 0.72	1.47	0.095 0.033 (0.069)	0.106 0.037 (0.081)	...	0.083 0.029	
A520	1.10 1280 (1123)	1.70 11.35	0.50 0.81	1.57	0.136 0.013 (0.138)	0.179 0.017 (0.168)	0.196 0.020 (0.174)	0.174 0.018	
A545	0.50 950 (914)	1.51 12.52	0.40 0.82	1.45	0.179 0.303 (0.182)	0.204 0.345 (0.199)	0.243 0.411 (0.193)	0.194 0.328	
A586	0.30 1150 (1275)	0.26 8.81	0.10 0.62	1.60	0.072 0.063 (0.083)	0.091 0.080 (0.105)	...	0.132 0.117	
A644	0.50 1100 (1110)	0.59 9.38	0.22 0.69	1.79	0.103 0.010 (0.119)	0.129 0.012 (0.139)	0.141 0.014 (0.151)	0.157 0.016	
A665	1.20 1350 (1170)	1.49 10.69	0.49 0.74	1.67	0.133 0.009 (0.135)	0.163 0.011 (0.166)	0.185 0.013 (0.175)	0.176 0.012	
A1068	0.25 915 (914)	0.42 9.72	0.12 0.70	1.36	0.102 0.025 (0.124)	0.119 0.030 (0.138)	...	0.146 0.037	
A1413	0.45 1140 (1137)	0.57 9.17	0.21 0.67	1.65	0.110 0.016 (0.122)	0.130 0.019 (0.145)	0.143 0.021 (0.161)	0.165 0.025	
A1651	0.40 940 (963)	0.58 9.01	0.22 0.66	1.50	0.127 0.006 (0.158)	0.156 0.008 (0.190)	0.191 0.012 (0.212)	0.213 0.014	
A1689	0.45 1300 (1233)	0.92 11.35	0.32 0.81	1.90	0.105 0.011 (0.126)	0.123 0.013 (0.132)	0.134 0.015 (0.129)	0.126 0.015	
A1763	0.75 1260 (1214)	1.16 9.20	0.40 0.66	1.64	0.090 0.006 (0.102)	0.123 0.008 (0.132)	0.146 0.010 (0.147)	0.150 0.011	
A1795	0.50 920 (947)	0.77 10.70	0.25 0.75	1.67	0.160 0.008 (0.172)	0.192 0.010 (0.183)	...	0.184 0.011	
A1835	0.25 1220 (1221)	0.32 10.22	0.09 0.72	1.55	0.112 0.024 (0.135)	0.124 0.027 (0.143)	...	0.154 0.034	
A2029	0.35 1070 (1137)	0.38 8.83	0.12 0.62	1.70	0.121 0.004 (0.152)	0.158 0.006 (0.185)	0.194 0.008 (0.215)	0.227 0.011	
A2142	0.50 1130 (1189)	0.61 8.57	0.19 0.60	1.79	0.145 0.019 (0.164)	0.190 0.025 (0.208)	0.237 0.031 (0.239)	0.255 0.033	
A2163	1.60 1680 <sup>†</sup> (1448)	1.09 9.16	0.36 0.65	1.96	0.164 0.010 (0.120)	0.194 0.012 (0.154)	0.203 0.014 (0.172)	0.183 0.014	
A2204	0.30 1150 (1183)	0.39 9.25	0.12 0.66	1.65	0.117 0.029 (0.137)	0.151 0.037 (0.160)	0.162 0.040 (0.179)	0.185 0.046	
A2218	0.70 1100 (1039)	0.99 10.32	0.30 0.70	1.52	0.125 0.005 (0.135)	0.157 0.007 (0.156)	0.184 0.009 (0.162)	0.162 0.008	
A2219	1.30 1600 (1373)	1.59 11.51	0.48 0.79	1.97	0.142 0.009 (0.130)	0.171 0.011 (0.154)	0.180 0.011 (0.157)	0.155 0.011	
A2244	0.35 920 (1039)	0.39 8.40	0.11 0.59	1.50	0.123 0.063 (0.133)	0.163 0.083 (0.171)	...	0.204 0.104	
A2256	1.60 1150 (1039)	2.34 13.60	0.56 0.82	1.87	0.151 0.019 (0.173)	0.209 0.024 (0.204)	0.216 0.025 (0.202)	0.196 0.023	
A2319	1.00 1200 (1189)	1.06 8.77	0.35 0.62	1.90	0.148 0.006 (0.150)	0.195 0.008 (0.199)	0.227 0.011 (0.226)	0.242 0.013	
A2390	0.65 1300 (1299)	0.64 9.25	0.24 0.67	1.70	0.151 0.021 (0.126)	0.175 0.024 (0.150)	0.202 0.029 (0.164)	0.169 0.024	
A2507	1.50 1240 (1195)	2.63 12.53	0.69 0.79	1.63	0.088 0.023 (0.081)	0.133 0.035 (0.105)	0.140 0.038 (0.111)	0.111 0.030	
A2744	3.80 1950 <sup>†</sup> (1293)	2.76 15.21	0.62 0.86	1.71	0.162 0.013 (0.121)	0.187 0.014 (0.141)	...	0.132 0.010	
A3112	0.23 700 (790)	0.26 8.68	0.08 0.60	1.17	0.171 0.088 (0.200)	0.230 0.118 (0.258)	...	0.277 0.143	
A3266	1.40 1200 (1103)	2.83 13.77	0.86 1.01	1.93	0.111 0.007 (0.160)	0.185 0.011 (0.199)	0.204 0.012 (0.204)	0.199 0.013	
A3888	0.80 1280 (1170)	0.68 9.35	0.24 0.67	1.66	0.123 0.025 (0.129)	0.145 0.029 (0.153)	...	0.170 0.035	
IRAS 09104	0.06 1100 (1137)	0.18 10.09	0.09 0.69	1.12	0.063 0.038 (0.089)	0.082 0.049 (0.102)	...	0.106 0.064	
MS 1358	0.40 1100 (1068)	1.48 14.29	0.35 0.87	1.45	0.088 0.075 (0.097)	0.117 0.101 (0.095)	...	0.086 0.074	
MS 2137	0.25 930 (889)	0.18 11.48	0.09 0.81	1.08	0.153 0.049 (0.191)	0.150 0.048 (0.188)	...	0.189 0.061	
PKS 0745	0.45 1200 (1150)	0.36 9.25	0.11 0.65	1.68	0.143 0.025 (0.115)	0.158 0.028 (0.135)	0.179 0.032 (0.153)	0.160 0.029	
Triang. Aus.	1.00 1300 (1239)	1.41 10.40	0.48 0.75	2.15	0.115 0.012 (0.126)	0.156 0.016 (0.155)	0.172 0.018 (0.165)	0.169 0.020	
Zw 3146	0.20 1310 (1311)	0.19 10.26	0.07 0.74	1.47	0.094 0.044 (0.125)	0.106 0.049 (0.140)	...	0.159 0.074	

cent uncertainty on  $f_{\text{gas}}$  is obtained by propagating the errors on the gas mass and total mass. The former are obtained in the deprojection analysis, by perturbing the surface brightness profile 100 times, according to the Poisson error on the counts in each radial bin. The uncertainty on the gravitating mass comes from assuming the above dependence upon the gas temperature,  $M_{\text{tot}} \propto T_{\text{gas}}^{3/2}$ , and propagating the relative error on the temperature itself, i.e.  $\epsilon(M_{\text{tot}})/M_{\text{tot}} = 1.5\epsilon(T_{\text{gas}})/T_{\text{gas}}$ .

To quantify the deviation between the deprojected and fitted results, we calculate at  $R_{\text{out}}$  for each cluster the quantity  $(f_{\text{gas,DEPROJ}} - f_{\text{gas,FIT}})/\epsilon(f_{\text{gas}})$ . On the sample of 36 clusters, we measure a median deviation of  $+0.48\epsilon(f_{\text{gas}})$ , with a range of  $-1.93, +2.81$ . The largest deviation is due to A2744, which shows a minor merger in the X-ray image and strong disagreement between the X-ray temperature and optical dispersion when isothermality is assumed.

#### 4.1 Comparison with previous work

Our sample of clusters with high X-ray luminosity contains several clusters already analyzed, with the *Einstein* and *ROSAT* HRIs. Only 6 of them have been studied also with the PSPC (i.e. A401, A1795, A2029, A2163, A2256, A2390).

We recall that the use of PSPC profiles extracted to about 2 Mpc (i) does not allow a good resolution in the inner part of the clusters, both in the deprojection analysis and in the fitting procedure, where we also cut the profile below 0.2 Mpc (or 0.1  $r_{500}$ ) to avoid the contribution from any cooling flow, and (ii) mainly weights the outskirts in the fitting analysis (just a few bins are located in the core). These points have to be borne in mind when we compare our results on the gas fraction measured in the inner part (e.g 500 kpc) with estimates obtained through observations

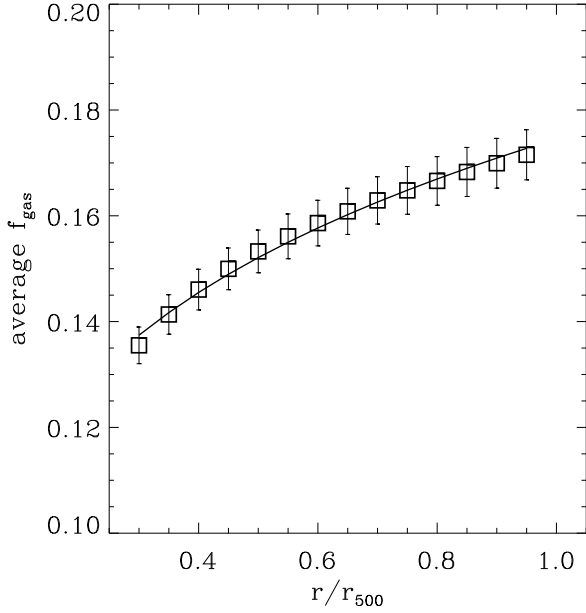


**Figure 10.** The average at different radii of  $f_{\text{gas}}$  from all 30 clusters with the respective error. We overplot the best-fit power law (index of  $0.20 \pm 0.02$ ;  $\chi^2 = 0.77$  for 12 degrees-of-freedom).

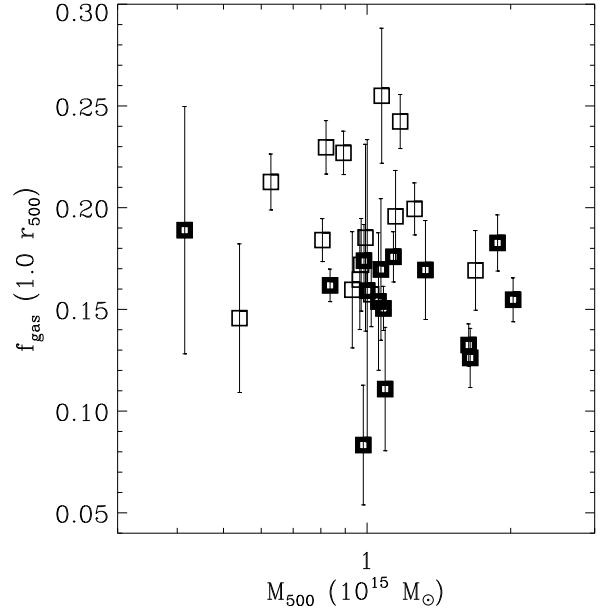


**Figure 12.** The gas fraction at  $r_{500}$  is shown with the corresponding gravitating mass at the same radius. The clusters at high redshift, with respect to the median value, are the solid symbols.

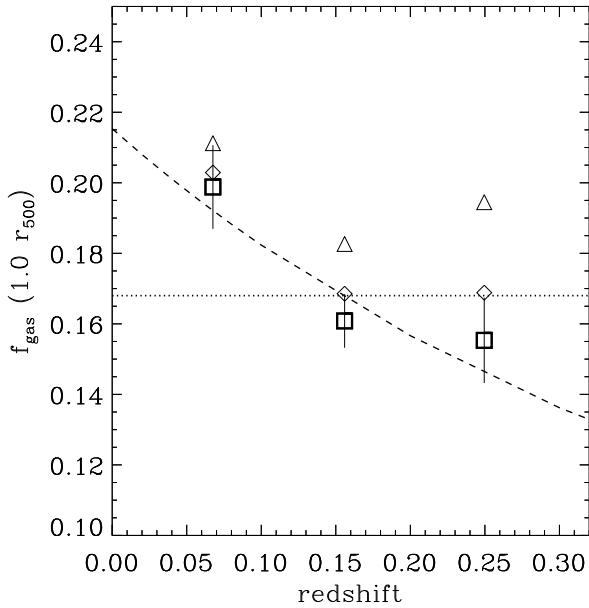


**Figure 11.** This plot shows the dependence of  $f_{\text{gas}}$  on the redshift with the best-fit result of  $0.215(-0.019, +0.020) (1+z)^{-1.75(-0.65, +0.65)}$  ( $\chi^2 = 1.62$ , with 1 degrees-of-freedom). The  $x$ -position of the bins is a biweight location. The  $y$ -position is the biweighted value with the respective error. When a different cosmology is considered into the dependence of  $f_{\text{gas}}$  upon  $d_{\text{ang}}^{1.5}$ , we obtain the values represented with *diamond* ( $\Omega_{0,m} = 0.2, \Omega_{\Lambda} = 0$ ) and *triangle* ( $\Omega_{0,m} = 0.2, \Omega_{\Lambda} = 1 - \Omega_{0,m}$ ). The dotted line represents the central value of  $f_{\text{gas}}$  from the robust analysis on 30 clusters.

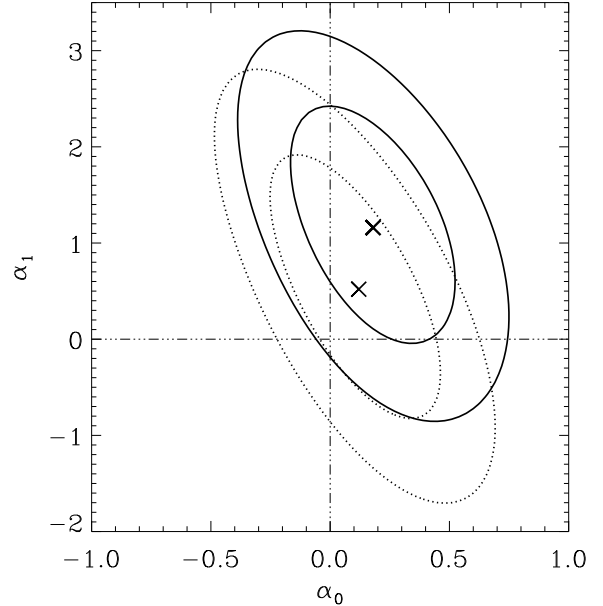


**Figure 13.** Error contours (68 and 95 per cent confidence, i.e.  $\Delta\chi^2 = 2.30, 6.17$ ) for the two interesting parameters  $\alpha_0$  and  $\alpha_1$  in equation 6. *Solid line:*  $\Omega_{0,m} = 1$ ; *dotted line:*  $\Omega_{0,m} = 0.2, \Omega_{\Lambda} = 1 - \Omega_{0,m}$ .

which are more efficient for that purpose (cf. the results from HRI observations in Allen & Fabian 1998).

In Fig. 6, we plot the difference in standard deviations between previous estimates and our results from the fitting procedure. We generally underestimate the gas fraction in the core of cooling flow clusters (e.g. A478, A1689, A1835, A2029, A2142) when compared to the Allen & Fabian (1998) results.

In A1795, the effect of the cooling flows produces a remarkable mismatch between our estimates and the results of David et al. (1995; about  $3.7\sigma$ ) and Allen & Fabian (1998;  $\sim 5.5\sigma$ ). On the other hand, the conclusion from Briel & Henry (1996) shows an opposite trend with respect to these and to our result from the fitting procedure, while White et al. (1997) are in good agreement with our value at 1 Mpc.

## 4.2 The distribution of $f_{\text{gas}}$ and its dependence upon redshift

We select from our sample the clusters where the value of  $f_{\text{gas}}(< r_{500})$  is twice its uncertainty, i.e. we apply the selection criterion that  $f_{\text{gas}}/\epsilon(f_{\text{gas}}) > 2$  (Fig. 7). This leaves 30 clusters (A545, A586, A2244, A3112, IRAS09104, MS1358, excluded) as our definitive sample. As discussed in Sect. 2, this sample is not complete in any sense. In the following analysis, we adopt the null hypothesis that (i) the gas fraction is constant with redshift and total mass, (ii) our high X-ray luminosity clusters are a homogeneous sample where no contamination is expected by, say, cooling flows. (Note that the gas temperatures are obtained from spectral analyses which exclude the cooling flow regions.)

The weighted mean of the values of  $f_{\text{gas}}(r_{500})$  is  $0.176(\pm 0.003)$ , with a variance of 0.037.

The mean, however, is statistically a poor estimator, being sensitive to (i) the replacement of even a small part of the data with different values, (ii) the assumed underlying population, (iii) the increase in the number of data to get better information. In this sense, the median is certainly a better estimator. But, an even better (i.e. more resistant, robust and efficient) estimator is the biweight location (Beers, Flynn & Gebhardt 1990). Using this estimator, we calculate  $f_{\text{gas}}(< r_{500}) = 0.171 \pm 0.035$ . Moreover, we can use the clusters where a significant cooling flow is present (cf. Table 1 in Allen & Fabian 1998) to estimate the gas mass fraction characteristic of more relaxed systems. We select 13 clusters (A478, A1068, A1413, A1689, A1795, A1835, A2029, A2142, A2204, A2390, MS2137, PKS0745, Zw3146) and measure a biweight of  $0.168 \pm 0.030$ , that is consistent with the distribution in the whole sample.

Both the weighted mean and our estimate of the biweight location are completely consistent with the biweight estimate of the gas fraction, at  $r_{500}$ , of  $0.170 \pm 0.008$  quoted by Evrard (1997) and calculated from two different published samples (White & Fabian 1995, David et al. 1995) after revision of the total mass of the David et al. clusters.

We now verify if the independent measurements of  $f_{\text{gas}}$  are compatible in a significant way. Applying the  $\chi^2$  test to our sample of  $f_{\text{gas}}$ , we find that these are *not* compatible at the  $> 99.9$  per cent confidence level when the weighted mean is adopted as the representative value. In fact, the deviations between our values of  $f_{\text{gas}}(r_{500})$  can be up to a factor of 3 (cf.

A483 and A2142; see also conclusions on A1060 and AWM7 in Loewenstein & Mushotzky 1996).

Carrying over our robust approach to these statistical issues, we investigate the compatibility between each value of  $f_{\text{gas}}$  and its average representative estimate, following the considerations in Press (1996) on the Bayesian combination of apparently incompatible measurements of the underlying quantity (in our case,  $f_{\text{gas}}$ ). This method, which weighs a weighted sum of ‘good’ and ‘bad’ Gaussians attributed to each measurement with an a priori probability that the experiment is ‘correct’, provides a distribution of probability for the value under investigation and a judgment on the goodness of each experiment. Applying it, we find that all the measurements, with a significantly low probability of less than 0.01 per cent that they are all wrong, are consistent with a distribution, roughly symmetric, peaked at 0.168 and with a dispersion of  $[-0.030, +0.036]$  (Fig. 8). This distribution is completely consistent with the biweight location and scale. Hereafter, we consider this value, with the respective “dispersion” around the “mean”, as the representative estimate of  $f_{\text{gas}}$  in our sample. In Fig. 8, we also indicate the estimated value of  $\Omega_b$  from low D abundance. When we compare this value with the calculated probability distribution of  $f_{\text{gas}}(r_{500})$ , we locate it on the wing of the distribution as very unlikely (probability of 0.7 per cent).

We investigate now two other issues related to the distribution of gas in clusters: (i) the dependence of the gas fraction on the radius within each cluster, and (ii) its constancy with the cosmological time. These issues are strictly related to the formation and evolution of clusters of galaxies in the present cosmological scenario.

The observed structure in the Universe results from the evolution of gravitational instability. On scales between  $10^{13}$  and  $10^{15} M_{\odot}$ , gravity is assumed to be the only force driving the formation of groups, poor clusters and clusters of galaxies. In this scenario, where the evolution is an entirely self-similar process, the gas and the total mass should have the same distribution.

This is not what is generally observed. In clusters, data analysis (e.g. White & Fabian 1995 and David, Jones & Forman 1995) and hydrodynamics simulations (Evrard 1997) show an increase of  $f_{\text{gas}}$  with radius. A way to explain the discrepancy between the distribution of gas and the underlying dark matter is to take into account physical phenomena able to redistribute the energy in the cluster, like galactic winds, ram-pressure stripping and heat input by supernovae type II (Evrard 1997, Metzger & Evrard 1998, Cavaliere, Menci & Tozzi 1998, Wu, Fabian & Nulsen 1998). In particular, the role of galactic winds is now well-studied in raising the gas entropy from the value achieved after gravitational collapse and flattening the gas distribution inside the cluster. This should affect both the global value of  $f_{\text{gas}}$  and its radial dependence.

In our case, which selects high-luminosity clusters, the median value of  $T_{\text{gas}}$  of 9 keV should save our local  $f_{\text{gas}}$  estimates from dropping significantly with respect to the global value. Feedback from galaxy formation affects the low-temperature clusters most strongly (e.g. Metzger & Evrard 1998), where the total intracluster thermal energy becomes comparable to the energy input from feedback.

On the other hand, we can investigate the redistribution of cluster energy, describing the radial variation of the

**Table 3.** The biweight values of  $f_{\text{gas}}$  (with the respective bootstrap error) for different subsamples selected, first, in redshift with respect to the median value of 0.1680, and then in  $M_{500}$  (the median values for the low and high redshift sample are 0.97 and  $1.08 \times 10^{15} M_{\odot}$ , respectively). In parenthesis, the number of values for each subsample is quoted.

	low $z$	high $z$
low $M_{500}$	$0.189 \pm 0.020$ (7)	$0.167 \pm 0.012$ (7)
high $M_{500}$	$0.192 \pm 0.017$ (8)	$0.151 \pm 0.012$ (8)

gas fraction. In Fig. 9, we show the general increase in  $f_{\text{gas}}$  when calculated at 0.3 and 1.0  $r_{500}$ . To quantify this trend, we collect in 14 radial bins equally spaced between  $[0.3, 1.0]$   $r_{500}$  the averaged gas fraction (with an error on the mean obtained from the propagation of the individual errors), making a composite  $f_{\text{gas}}$  profile. Then, fitting a power law to the 14 bins (Fig. 10), we obtain  $f_{\text{gas}}(r) \propto (r/r_{500})^{0.20 \pm 0.02}$ . This result is slightly steeper than the estimate of about 0.13–0.17 from simulations (cf. Evrard 1997).

Moreover, in the two clusters (A644, A1651) for which the radius where a dark matter overdensity of 200 is surveyed (i.e.,  $r_{200} < R_{\text{out}}$ ), we observe that the gas fraction increases by about a further 15 per cent from  $r_{500}$  to  $r_{200}$ .

The evidence of a positive gradient underlines a lower concentration of the gas with respect to the dark mass, that is consequence of both our assumption on the dark matter profile (at  $r \sim r_{500}$ ,  $\rho_{\text{DM}} \propto r^{-2.4}$ ; cf. N-body simulations results, for example Thomas et al. 1998) and our best-fit results on the slope of the gas density (i.e.  $\rho_{\text{gas}} \propto r^{-3\beta} \propto r^{-2.2}$ , that implies a dependence of  $M_{\text{gas}}$  on  $r^{0.8}$ ). In other words, converting the dependence of the gas fraction upon radius to a dependence on the different mass components, we conclude that  $f_{\text{gas}}(r) \propto [M_{\text{gas}}(r)/M_{\text{gas}}(r_{500})]^{1/4} \propto [M_{\text{tot}}(r)/M_{500}]^{1/3}$ .

Another argument against simple self-similar cluster evolution would be a variation of  $f_{\text{gas}}$  with redshift.

First, the use of Spearman’s rank-order correlation shows that  $f_{\text{gas}}$  is correlated with redshift at a confidence level  $> 99$  per cent. We investigate this further by dividing the sample according to the median value in redshift ( $z=0.1680$ ) and calculating the biweight location (and respective bootstrap error) of the  $f_{\text{gas}}(r_{500})$  values. We obtain  $0.192(\pm 0.012)$  and  $0.159(\pm 0.009)$ , at low and high redshifts, respectively. The evidence of a higher local gas fraction is also clear from Fig. 11, where we sample the data in 3 redshift bins of 10 elements each. Each bin is represented with the biweight location, and the respective error. We fit then a power law,  $f_{\text{gas},0} \times (1+z)^{-\alpha}$ , and measure  $f_{\text{gas},0} = 0.215(-0.019, +0.020)$  and  $\alpha = 1.75(-0.65, +0.65)$ , where the errors are  $1\sigma$  deviation. Again, the slight negative evolution in the gas fraction appears significant at  $\sim 2.7\sigma$  level (estimated from the value of  $\alpha$  and its error).

We have also looked for trends of  $f_{\text{gas}}$  with the total mass,  $M_{500}$ , (Fig. 12) considering the biweight gas fraction values calculated in subsamples that were selected according to the median of the redshifts and of the masses (Table 3). In particular, we search for the minimum in the  $\chi^2$  distribution, when the data in Table 3 are compared with the model

$$f_{\text{gas}}(r_{500}) = \text{const} \times M_{500}^{-\alpha_0} (1+z)^{-\alpha_1}. \quad (6)$$

We obtain a minimum  $\chi^2$  of 0.39 (one d.o.f.) with the best-fit

parameters:  $\alpha_0 = 0.15$ ,  $\alpha_1 = 1.24$ . In Fig. 13, we plot the 68 and 95 per cent errors contour for the two slope parameters. The dependence on the redshift is well in agreement with the previous results plotted in Fig. 11. On the other hand, there is no evidence for any statistically significant dependence of  $f_{\text{gas}}(r_{500})$  on  $M_{500}$ .

Allen & Fabian (1998) show a decrease in the gas fraction of clusters at higher temperature (cf. their Fig. 3). If we replace  $M_{500}$  in equation 6 with the intracluster temperature, we find that the slope of  $T_{\text{gas}}$  is within the range  $[-1.4, 0.4]$  at the 95 per cent confidence level. But putting  $\alpha_1 = 0$ ,  $\alpha_0$  has to be larger than 0 (95 per cent c.l.), in agreement with Allen & Fabian results.

We also note that, from the scaling law between mass and temperature ( $M \propto T_{\text{gas}}^{3/2}$ ), any apparent dependence of  $f_{\text{gas}}$  upon  $T_{\text{gas}}$  becomes weaker by a factor 2/3 when applied to mass.

This scenario implies that the gas component in the X-ray highly-luminous systems considered here is almost independent of the mass and only slightly on the temperature, once the redshift dependence is taken into account.

Any apparent decrease with redshift of the gas fraction, however, has been recently questioned. Following an original idea of Sasaki (1996), Cooray (1998) and Danos & Pen (1998; see also Rines et al. 1998) have shown the angular distance–redshift relation,  $d_{\text{ang}}(z, q_0)$ , that we write in equation 3, to be the major factor responsible for the apparent negative evolution. From the definition of the gas fraction, it holds that  $f_{\text{gas}} \propto d_{\text{ang}}^{3/2}$  and, consequently,  $f_{\text{gas}}$  tends to be lower at higher redshifts in a high density universe.

We consider the changes in  $f_{\text{gas}}$  for cosmologically different scenarios in Fig. 11. We lower  $\Omega_{0,m}$  to 0.2, applying both an open universe and a flat one with a cosmological constant  $\Omega_{\Lambda} = 1 - \Omega_{0,m}$  [cf. eqn. (25) in Carroll, Press & Turner 1992]. In the latter case the change appears more significant in flattening  $f_{\text{gas}}$  to a non-evolving value. Fitting a power-law to these values, we obtain  $f_{\text{gas}} = 0.210(-0.020, +0.022) \times (1+z)^{-0.61(-0.66, +0.64)}$  with a reduced  $\chi^2$  of 1.3. All the errors are one standard deviation.

Also when we apply equation 6 to the case  $[\Omega_{0,m}, \Omega_{\Lambda}] = [0.2, 0.8]$ , that shows the better agreement with the constant  $f_{\text{gas}}$  assumption, we observe a significant flattening in the redshift dependence. The best-fit parameters ( $\chi^2 = 0.22$  for 1 d.o.f.) are now  $(\alpha_0, \alpha_1) \sim (-0.1, 0.5)$ , with a range for the  $\alpha_0$  values of  $[-0.5, 0.7]$  at the 95 per cent confidence level (dotted contours in Fig. 13).

Thus, a low density Universe not only matches the observed gas fraction with the baryonic amount provided during the primordial nucleosynthesis, but also flattens to a constant (in look-back time) gas mass fraction of about 0.196 (biweight estimate).

### 4.3 The dependence of $f_{\text{gas}}$ on the temperature profile

In this Section, we remark on the role of a negative gas temperature gradient (instead of an isothermal profile) in estimating the cluster gas fraction. Markevitch et al. (1998) have recently claimed, from the analysis of a sample of clusters observed from the X-ray satellite *ASCA*, that a negative temperature gradient is generally present and well represented by a polytropic function with index,  $\gamma$ , of 1.2–1.3

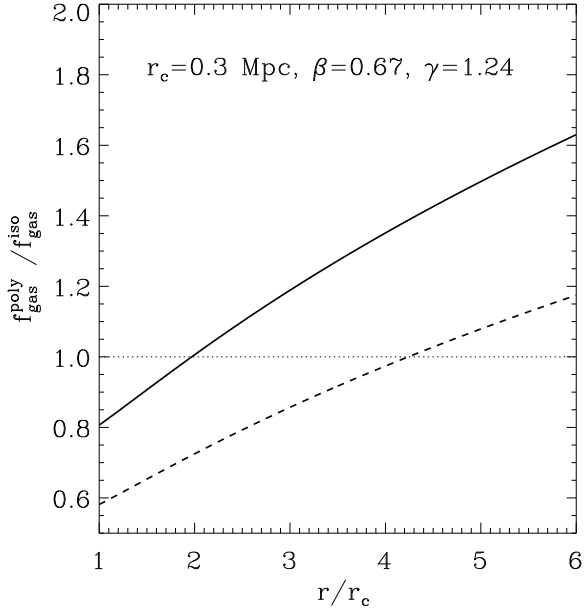


**Figure 14.** The gas fraction relative to the isothermal case, after correction for the gradient in the temperature parametrised by the polytropic equation (see Appendix). When we assume the isothermal gas temperature equal to the maximum value of the temperatures allowed from the polytropic profile (i.e. the central value,  $T_0$ ), we observe an increase of the polytropic  $f_{\text{gas}}$  estimate up to 60 per cent with respect to the isothermal  $f_{\text{gas}}$  value at  $r \sim 6r_c$  (solid line). Using an emission-weighted average of the temperatures spanned from the polytropic profile as reference value for the isothermal profile (instead of the central value), the correction on  $f_{\text{gas}}$  is by about 17 per cent at the same radius (dashed line).

between 1 and 6 X-ray core radii. They have assumed a  $\beta$ -model with  $[\beta, r_c]$  of  $[0.67, 0.3 \text{ Mpc}]$  to constrain the gas density, and then used the polytropic equation to fit the temperature profiles.

In the Appendix, we derive the equations necessary to describe the polytropic state of the intracluster plasma. Using the results of Markevitch and collaborators, we make a correction to the total mass via equation A9 of about 1.2 – 0.6 over the radial range  $[1, 6]r_c$  on the total mass. It yields a larger gas fraction with respect to the isothermal case, above  $2 r_c$ . At  $r \sim 6 r_c \sim r_{500}$ , the polytropic value of  $f_{\text{gas}}$  can be larger by a factor of 1.6 than the isothermal estimate (Fig. 14).

We have also fitted eqn. A7–A5 to the profiles of the 34 clusters in our sample with enough data points, to obtain  $\gamma = 1.25 \pm 0.13$ . None of these polytropic fits, however, is better than the isothermal one at 95 per cent confidence level using the F-test.

We note that steep electron temperature profiles need not be representative of the state of the gas. As shown by, e.g., Ettori & Fabian (1997) and Takizawa (1998), the efficiency of the Coulomb collisions between ions and electrons has to be considered when a such negative gradient is observed in clusters, even if they underwent an ancient merger. Thus, when the equipartition time is comparable to the age of the last, large, merging event, it is also true that the

mean gas temperature profile *is generally flatter* than the (emission-weighted) electron temperature profile estimated from X-ray observations.

In conclusion, the presence of a non-isothermal temperature profile tends to increase the gas fraction value at  $r_{500}$ , more or less significantly depending on our underestimate of the drop of the temperature in the outskirts of each cluster with respect to the assumed representative isothermal value. Whether this is a systematic or random uncertainty in our results depends upon whether all clusters have similar profiles or not up to  $r_{500}$ . Current data are unable to clarify this important issue.

## 5 $\Omega_{0,M}$ FROM THE GAS FRACTION

The range of observed cluster gas fractions can now be compared with the results of primordial nucleosynthesis calculations. Assuming that the current best estimate for  $H_0 = 73 \pm 14 \text{ km s}^{-1} \text{ Mpc}^{-1}$  (Freedman et al. 1998), and the constraint

$$\Omega_{0,m} < \frac{\Omega_b}{f_{\text{gas}}} \left( \frac{H_0}{50 \text{ km s}^{-1} \text{ Mpc}^{-1}} \right)^{-0.5}, \quad (7)$$

we obtain  $\Omega_{0,m} < 0.20(-0.13, +0.13)$ , adopting  $\Omega_b = 0.04$  which corresponds to the high deuterium abundance estimate, and  $\Omega_{0,m} < 0.37(-0.16, +0.09)$ , using  $\Omega_b = 0.076$ . The error bars come from the propagation of the accepted range for the given  $\Omega_b$  (see beginning of Sect. 4). From the latter estimate, we can put an upper limit on the density of the Universe as inferred from the measured gas fraction in our sample of highly-luminous clusters:  $\Omega_{0,m}$  has to be less than 0.56 at the 95 per cent confidence level. We note that our estimate for  $\Omega_{0,m}$  is conservative due to our use of an ‘average’ value for  $f_{\text{gas}}$ . If we adopt the 95 per cent lower limit to the highest reliable values in our sample of gas fraction (considering 10 per cent of the sample, that of A2142, A2319, A401, A2029) to constrain the cosmological parameter, we require that  $\Omega_{0,m} < 0.34$ .

Using the conservative constraint, it is straightforward to require  $\Omega_\Lambda = 1 - \Omega_{0,m} > 0.44$  (95 per cent confidence level), still marginally consistent with the recent results on the magnitude-redshift relation for the type Ia supernovae (Perlmutter et al. 1998).

We have neglected so far any other baryonic contribution, like galaxies and baryonic dark matter. The luminous mass in galaxies is about a fifth of the gas fraction, i.e.  $g = f_{\text{gal}}/f_{\text{gas}} \sim 0.2h_{50}^{1.5}$  (White et al. 1993, Fukugita et al. 1998). The cluster baryonic dark matter is suggested to be in the form of cold clouds or low mass stars and brown dwarfs deposited by cooling flows (Thomas & Fabian 1990, Fabian 1994). Also on galactic scale, low mass dark objects can be deposited by a cooling flow in the halo during first collapses of a protogalaxies (Nulsen & Fabian 1997).

The last equation can be then rewritten considering these other baryonic contributions. Defining  $b$  as the ratio of this baryonic dark matter to the gas fraction, and assuming it is independent of  $H_0$ , we can write:

$$\Omega_{0,m} = \frac{\Omega_b}{f_{\text{gas}}} \frac{h_{50}^{-0.5}}{1 + (b + g)h_{50}^{1.5}}. \quad (8)$$

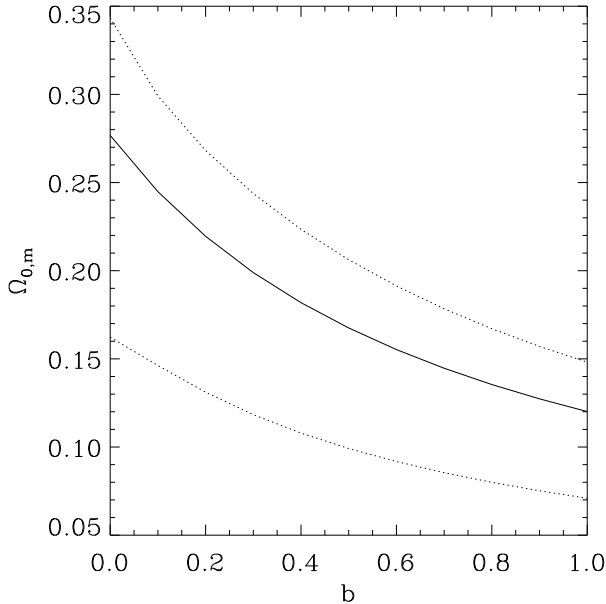


**Figure 15.** Expectation values for  $\Omega_{0,m}$  when a baryonic contribution is considered in addition to intracluster gas and stars in galaxies [cf. equation 8]. The case  $b = 0$  corresponds to the  $\Omega_{0,m}$  value estimated considering only  $f_{\text{gas}}$  and assuming a low value for D/H.

For different  $b$  values, using the best estimates from our previous analysis and propagating the errors as usual, we plot in Fig. 15 the estimated  $\Omega_{0,m}$  with  $1\sigma$  uncertainty. For example, recent estimate on the universal primordial baryon fraction from MACHO results (Steigman & Tkachev 1998), assumed baryonic and in the halo of the Galaxy, give us a value of  $b \sim 0.6$ , with a consequent  $\Omega_{0,m}$  of about 0.15.

Here we note that the contribution from baryonic dark matter can be about 3 times the luminous matter in normal stars, as predicted from standard model of gas processes in galactic formation (Nulsen & Fabian 1997). This can partially explain the large scatter in the gas fraction distribution (for example, cf. Fig. 12), suggesting that most of the baryons in clusters with lower values of  $f_{\text{gas}}$  are in the form of dark matter.

## 6 SUMMARY AND CONCLUSIONS

In our sample of 30 hot (median  $T_{\text{gas}} = 9$  keV) and intermediate distance (median  $z = 0.1680$ ) clusters of galaxies, we have applied both the deprojection technique and the fitting approach, using both (a) the  $\beta$ -model and (b) a gas profile obtained from the Navarro-Frenk-White potential. For (a) we find that the median best-fit parameters are  $[\beta, r_c] = [0.71, 0.24$  Mpc]; for (b),  $[\eta, r_s] = [10.20, 0.75$  Mpc].

The two techniques produce the same values of  $f_{\text{gas}}$  within a median deviation of less than  $1\sigma$ .

Assuming an isothermal profile for the gas temperature, with the caveats discussed in Sect. 4.3 on the role played by a decrease of the temperature outward, we obtain the following results on the gas fraction,  $f_{\text{gas}}$ :

(i) At the radius where the cluster overdensity is 500, the measured values of  $f_{\text{gas}}$  have a biweight location and scale of  $0.171 \pm 0.035$ . When Bayesian statistics are adopted, the probability distribution is peaked at 0.168 and has a 95 per cent range of  $[0.101, 0.245]$  (Fig. 8).

With respect to this distribution, the highest estimate of  $\Omega_b$  (corresponding to a low deuterium abundance) has a probability of  $7.2 \times 10^{-3}$  in an Einstein-de Sitter Universe ( $\Omega_{0,m} = 1$ ).

When we consider the more relaxed clusters with a central cooling flow, we measure  $0.168 \pm 0.030$ .

If we consider the cosmological correction in the angular size-redshift relation for a flat Universe with  $\Omega_\Lambda = 0.8$ , we measure the biweight values of  $0.196 \pm 0.035$ .

(ii) Many of the individual estimates of  $f_{\text{gas}}$  are inconsistent with the average value or with each other, confirming that there are real differences in the measured gas fractions in clusters (Fig. 7, 9, 12). It remains possible that some of this spread is due to a breakdown in our assumptions. There may, for example, be a merger taking place along the line of sight in some clusters. If the gas is actually more extended along the line-of-sight then we have underestimated the gas fraction, conversely if it is foreshortened then the gas fraction is overestimated.

(iii) The average dependence upon the radius within a cluster is  $r^s$ , with  $s \sim 0.20$  (Fig. 10). This follows from our best-fit results on the slope of the gas density,  $\rho_{\text{gas}} \propto r^{-2.2}$ , and our assumption of the Navarro-Frenk-White functional form for the dark matter distribution. In general, we can write  $f_{\text{gas}} \propto r^{-2.2-s_{\text{DM}}}$ , where  $s_{\text{DM}}$  is the slope of the dark matter profile.

(iv) In our sample of high-luminosity clusters, there is a highly significant correlation between  $f_{\text{gas}}(r_{500})$  and redshift, that we quantify fitting the function  $f_{\text{gas},0} \times (1+z)^{-\alpha}$ :  $f_{\text{gas},0} = 0.215^{+0.020}_{-0.019}$ ,  $\alpha = 1.75 \pm 0.65$  ( $\Omega_{0,m} = 1$ ). When we take it into account, there is then only a mildly significant dependence of  $f_{\text{gas}}(r_{500})$  upon the temperature (and, even weaker, upon the mass). The dependence upon redshift weakens (i.e. the significance of any decrease in  $f_{\text{gas}}$  is reduced) in a low matter density universe, in particular if a cosmological constant is present. The normalization of the power law, i.e. the extrapolated local value of the gas fraction,  $f_{\text{gas},0}$ , remains stable at 0.21.

(v) Adopting both a low and a high abundance for deuterium and requiring that any physical source in redistributing the energy within the cluster cannot produce large variations in the value of  $f_{\text{gas}}$  quoted above [cf. (i)], we constrain  $\Omega_{0,m} < 0.56$  at the 95 per cent confidence level. If we take the highest significant estimates of  $f_{\text{gas}}$  in our cluster sample, we find that  $\Omega_{0,m} < 0.34$ .

(vi) Future X-ray missions can constrain better the temperature gradient in the electron (and electron+ion) population. If the indication of a negative gradient in  $T_{\text{gas}}$  is confirmed,  $f_{\text{gas}}$  rises and  $\Omega_{0,m}$  drops by a factor that can be, at maximum, 1.6. Such a large value of  $f_{\text{gas}}$  could become a real concern for the physics of the formation and evolution of clusters of galaxies in present cosmological scenarios.

## ACKNOWLEDGEMENTS

We are grateful to Steve Allen, Kelvin Wu, David White and Vince Eke for useful discussions. We thank the anonymous referee for comments which improved this work. SE acknowledges support from PPARC, Cambridge European Trust and *Alfred Toepfer Stiftung F.V.S.*, ACF the support of the Royal Society. This research has made use of data obtained through the High Energy Astrophysics Science Archive Research Center Online Service, provided by the NASA-Goddard Space Flight Centre.

## REFERENCES

- Allen S.W., Fabian A.C., 1998, MNRAS, 297, L57  
 Arnaud K.A., 1996, "Astronomical Data Analysis Software and Systems V", eds. Jacoby G. and Barnes J., ASP Conf. Series vol. 101, 17  
 Beers T.C., Flynn K., Gebhardt K., 1990, AJ, 100, 32  
 Briel U.G., Henry J.P., Böhringer H., 1992, A&A, 259, L31  
 Briel U.G., Henry J.P., 1996, ApJ, 472, 131  
 Böhringer H., Tanaka Y., Mushotzky R.F., Ikebe Y., Hattori M., 1998, A&A, 334, 789  
 Buote D.A., Canizares C.R., 1996, ApJ, 457, 565  
 Burles S., Tytler D., 1998, Space Science Reviews, 84 (1/2), 65  
 Carroll S.M., Press W.H., Turner E.L., 1992, ARAA, 30, 499  
 Cavaliere A., Fusco-Femiano R., 1976, A&A, 49, 137  
 Cavaliere A., Menci N., Tozzi, P., 1998, ApJ, 501, 493  
 Cooray A.R., 1998, A&A, 333, L71  
 Danos R., Pen U., 1998, astro-ph/9803058  
 David L.P., Slyz A., Jones C., Forman W., Vrtilik S.D., & Arnaud K.A., 1993, ApJ, 412, 479  
 David L.P., Jones C., Forman W., 1995, ApJ, 445, 578  
 Davis D.S., White III R.E., 1998, ApJ, 492, 57  
 de Vaucouleurs G., 1948, Ann. Astrophys., 11, 247  
 Durret F., Forman W., Gerbal D., Jones C., Vikhlinin A., 1998, A&A, 335, 41  
 Ebeling H., Voges W., Böhringer H., Edge A.C., Huchra J.P., Briel U.G., 1996, MNRAS, 281, 799  
 Elbaz D., Arnaud M., Böhringer H., 1995, A&A, 293, 337  
 Ettori S., Fabian A.C., White D.A., 1997, MNRAS, 289, 787  
 Ettori S., Fabian A.C., 1997, MNRAS, 292, L33  
 Ettori S., Fabian A.C., White, D.A., 1998, MNRAS, 300, 837  
 Evrard A.E., Metzler C.A., Navarro J.F., 1996, ApJ, 469, 494  
 Evrard A.E., 1997, MNRAS, 292, 289  
 Fabian A.C., 1991, MNRAS, 253, 29p  
 Fabian A.C., 1994, ARAA, 32, 277  
 Freedman W.L., Mould J.R., Kennicutt Jr R.C., Madore B.F., 1998, astro-ph/9801080  
 Fukazawa Y., Makishima K., Tamura T., Ezawa H., Xu H., Ikebe Y., Kikuchi K., Ohashi T., 1998, PASJ, 50, 187  
 Fukugita M., Hogan C.J., Peebles P.J.E., 1998, ApJ, 503, 518  
 Girardi M., Escalera E., Fadda D., Giuricin G., Mardirossian F., Mezzetti M., 1997, ApJ, 482, 41  
 Henriksen M.J., Markevitch M., 1996, ApJL, 466, L79  
 Hogan C.J., 1998, Space Science Reviews, 84 (1/2), 127  
 Hjorth J., Oukbir J., van Kampen E., 1998, MNRAS, 298, 1  
 Kaastra J.S., 1992, *An X-Ray Spectral Code for Optically Thin Plasmas* (Internal SRON-Leiden Report, updated version 2.0)  
 Liedahl D.A., Osterheld A.L., Goldstein W.H., 1995, ApJ, 438, L115  
 Loewenstein M., Mushotzky R. F., 1996, ApJL, 471, 83  
 Makino N., Sasaki S., Suto Y., 1998, ApJ, 497, 555  
 Malumuth E. M., Kirshner R.P., 1985, ApJ, 291, 8  
 Markevitch M., Mushotzky R., Inoue H., Yamashita K., Furuzawa A., Tawara Y., 1996, ApJ, 456, 437  
 Markevitch M., Vikhlinin A., ApJ, 1997, 491, 467  
 Markevitch M., Forman W.R., Sarazin C.L., Vikhlinin A., ApJ, 1998, 503, 77  
 Markevitch M., 1998, 504, 27  
 Metzler C.A., Evrard A.E., 1998, ApJ, submitted (astro-ph/9710324)  
 Navarro J.F., Frenk C.S., White S.D.M., 1995, MNRAS, 275, 720  
 Navarro J.F., Frenk C.S., White S.D.M., 1997, ApJ, 490, 493  
 Nulsen P.E.J., Fabian A.C., 1997, MNRAS, 291, 425  
 Owen F.N., Ledlow M.J., Morrison G.E., Hill J.M., 1997, ApJL, 488, L15  
 Perlmutter S. et al., 1998, Nature, 391, 51  
 Press W.H., Teukolsky S.A., Vetterling W.T., Flannery B.P., 1992, *Numerical Recipes*, Cambridge University Press  
 Press W.H., 1996, "Unsolved Problems in Astrophysics", Proceedings of Conference in Honor of John Bahcall, ed. J.P. Ostriker, Princeton University Press  
 Rines K., Forman W., Pen U., Jones C., Burg R., 1999, ApJ, in press (astro-ph/9809336)  
 Rottgering H.J.A., Wieringa M.H., Hunstead R.W., Ekers R.D., 1997, MNRAS, 290, 577  
 Rybicki G.B., Lightman A.P., 1979, *Radiative Processes in Astrophysics*, John Wiley & Sons, New York  
 Sarazin C.L., Wise M.W., Markevitch M.L., 1998, ApJ, 498, 606  
 Sasaki S., 1996, PASJ, 48, L119  
 Smail I., Ellis R.S., Dressler A., Couch W.J., Oemler A.Jr., Sharples R.M., Butcher H., 1997, ApJ, 479, 70  
 Snowden S.L., McCammon D., Burrows D.N., Mendenhall J.A., 1994, ApJ, 424, 714  
 Songaila A., Wampler E.J., Cowie L.L., 1997, Nature, 385, 137  
 Steigman G., Tkachev I., 1999, ApJ, in press (astro-ph/9803008)  
 Stewart G.C., Fabian A.C., Jones C., Forman W., 1984, ApJ, 285, 1  
 Struble M.F., Rodd H.J., 1991, ApJS, 77, 363  
 Takizawa M., 1998, ApJ, 509, 579  
 Thomas P.A., Fabian A.C., 1990, MNRAS, 246, 156  
 Thomas P.A. et al., 1998, MNRAS, 296, 1061  
 Walker T.P., Steigman G., Schramm D.N., Olive K.A., Kang H.S., 1991, ApJ, 376, 51  
 White D.A., Fabian A.C., 1995, MNRAS, 273, 72  
 White D.A., Jones C., Forman W., 1997, MNRAS, 292, 419  
 White S.D.M., Frenk C.S., 1991, ApJ, 379, 52  
 White S.D.M., Navarro J.F., Evrard A.E., Frenk C.S., 1993, Nature, 366, 429  
 Wu K.K.S., Fabian A.C., Nulsen P.E.J., 1998, MNRAS, 301, L20

## APPENDIX A: ANALYTIC MODELS FOR THE STATE OF THE INTRACLUSTER GAS

The Navarro, Frenk & White (NFW) density profile,  $\rho_{\text{NFW}} = \rho_s x^{-1}(1+x)^{-2}$ , generates a gravitational potential of the form:

$$\frac{d\phi}{dr} = 4\pi G r_s \rho_s \frac{\ln(1+x) - x/(1+x)}{x^2}, \quad (\text{A1})$$

where, defining  $r_s$  as a *scale* radius,  $x = r/r_s$  and  $\rho_s = \rho_c \delta_c (1+z)^3 \Omega_0/\Omega_z$ , with  $\delta_c$  equal to the characteristic density of the cluster and  $\rho_c$  to the critical density (see Appendix in Navarro, Frenk & White 1997).

Putting it in the hydrostatic equation, and assuming the isothermality for the intracluster gas,  $T_{\text{gas}}(r) = T_0$ ,

$$\frac{1}{\rho_{\text{gas}}} \frac{d\rho_{\text{gas}}}{dr} = -\frac{\mu m_p}{k T_{\text{gas}}} \frac{d\phi}{dr}, \quad (\text{A2})$$

we obtain



$$\rho_{\text{gas}} = \rho_0 e^{-\eta} (1+x)^{\eta/x} = a_0 (1+x)^{\eta/x}, \quad (\text{A3})$$

where

$$\eta = \frac{4\pi G \rho_s r_s^2 \mu m_p}{kT_0} = \frac{1.5\delta_c (1+z)^3 (\Omega_0/\Omega_z) H_0^2 r_s^2 \mu m_p}{kT_0}. \quad (\text{A4})$$

(we define, as usual,  $G$  as the Gravitational constant,  $\Omega_0$  and  $\Omega_z$  as the cosmological parameters at the present time and at redshift  $z$ , and  $H_0$  as the present-time Hubble constant). The gas density profile is then integrated and fitted to the observed surface brightness profile to constrain the free parameters  $\rho_0$ ,  $r_s$  and  $\eta$ . Hence, given  $T_0$  and the best-fit parameters  $r_s$  and  $\eta$ ,  $\delta_c = \bar{\delta}/3 \times c^3 / [\ln(1+c) - c/(1+c)]$  and the concentration parameter  $c$  can be estimated from eqn. A4. Here,  $\bar{\delta}$  is the mean interior overdensity that defines a cluster over the background. It is generally assumed equal to about 200, that is the density contrast of a virialized object in the nonlinear regime of spherical collapse.

The radius at which this mean overdensity is reached,  $r_{\bar{\delta}}$ , is then defined  $r_{\bar{\delta}} = c r_s$  (Navarro, Frenk & White 1995, 1997). NFW (1997) show that for a cluster identified at redshift  $z$ , the cosmological dependence of  $r_{\bar{\delta}}$  is  $(\Omega_0/\Omega_z)^{-1/3} (1+z)^{-1} = (1+\Omega_0 z)^{-1/3} (1+z)^{-2/3}$ . This decreases with the redshift and increases slightly with the lowering of the density parameter: for example, at redshift 0.4,  $r_{\bar{\delta}}$  is lower than the local estimate by about 29 and 23 per cent for  $\Omega_0$  equal to 1 and 0.3, respectively.

We can also generalize to an intracluster gas with a polytropic equation of state

$$\rho_{\text{gas}} = \rho_0 \left[ \frac{T_{\text{gas}}(r)}{T_0} \right]^{\frac{1}{\gamma-1}} \quad (\text{A5})$$

the consequences of the hydrostatic equilibrium with a cluster potential described by the NFW functional form (eqn. A1):

$$\frac{d(kT_{\text{gas}})}{dr} = \mu m_p \frac{\gamma-1}{\gamma} \left( -\frac{d\phi}{dr} \right), \quad (\text{A6})$$

that integrated over the radial range of interest provides the equation:

$$\frac{T_{\text{gas}}(r)}{T_0} = 1 + \eta \frac{\gamma-1}{\gamma} \left[ \frac{\ln(1+x)}{x} - 1 \right], \quad (\text{A7})$$

where  $T_{\text{gas}}(0) = T_0$  and  $\eta = \eta(T_0)$ .

The gas density profile is then obtained using equation A5.

The presence of a temperature gradient also affects the estimate of the total gravitating mass,  $M_{\text{tot}}$ , for which the gravitational potential is unknown:

$$M_{\text{tot}} = -\frac{kT_0 r^2}{\mu m_p G} \gamma \left( \frac{\rho_{\text{gas}}}{\rho_0} \right)^{\gamma-2} \frac{d}{dr} \left( \frac{\rho_{\text{gas}}}{\rho_0} \right). \quad (\text{A8})$$

The case  $\gamma = 1$  provides the usual equation to estimate the total gravitating mass when the gas is isothermal. In particular, the ratio between the polytropic and isothermal mass estimates will be given by

$$\frac{M^{\text{poly}}}{M^{\text{iso}}} = \gamma \left( \frac{\rho_{\text{gas}}}{\rho_0} \right)^{\gamma-1} = \gamma \frac{T_{\text{gas}}(r)}{T_0}. \quad (\text{A9})$$

This equation has been used to estimate the correction on  $f_{\text{gas}}$  for the presence of a temperature gradient as plotted in Fig. 14.